

Silicon Sensor Irradiation Studies for the Large Hadron Collider High Luminosity Upgrade



BROWN

Andrew Thomas Kent

Department of Physics

Brown University

Submitted in partial satisfaction of the requirements for the
Degree of Master of Science
in Physics

Advisor: Professor Ulrich Heintz

May 2022

© 2022 - Andrew Thomas Kent

All rights reserved.

*This thesis by Andrew Thomas Kent is accepted in its present form by the
Department of Physics as satisfying the thesis requirement for the degree of Master
of Science.*

.....
Date Ulrich Heintz, Advisor

Recommended to the Graduate Council

.....
Date Andrew G. Campbell, Dean of the Graduate School

To my parents, Zaida Soriano and Ron Kent.

Acknowledgements

I am very grateful to have had many people help me along the way in my pursuit of an education in physics, and I especially wanted acknowledge a few of those who especially helped me with my goals.

Before arriving at Brown University I received extensive mentoring from Distinguished Professor of Physics at UCLA, George Morales - we would meet every week for a few hours and he would teach me what it meant to be a theoretical physicist and how one should go about solving very difficult problems. I will always look back fondly on those meetings I had with him. While at UCLA I was also the recipient of the Nicholas Dieter Memorial Scholarship which was awarded by former U.S. Ambassador Robert J. Dieter and Mrs. Gwynneth Dieter, their kind words and support helped me quell many doubts I had about the future.

I would like to thank Professor Ulrich Heintz for allowing me to learn in his lab as a laboratory assistant and also for his guidance in writing this thesis, my time working in his lab has been a wonderful education. Also, from the Brown University Silicon Lab I would like to whole heartedly thank Eric Spencer and Nick Hinton. Eric taught me almost all of the techniques and skills I used in my research presented in this thesis, and I am very grateful for all his support.

Finally, I would like to thanks my family, friends and my girlfriend Yasemin Kiraç. I also want to especially thank my mother Zaida Soriano. At every step of the way she has supported me. When I decided to switch my path from cooking professionally to going back to school and pursuing physics she was my number one fan, and for that and an incomprehensible list of other supportive things she has done for me, I am eternally grateful to her. Mom, I love you.

Table of Contents

Dedication	iii
Acknowledgements	iv
1 Introduction	1
1.1 The Large Hadron Collider	1
1.1.1 The High-Luminosity Large Hadron Collider (HL-LHC)	1
1.2 The Compact Muon Solenoid Experiment at CERN	3
1.2.1 Silicon Sensors	4
1.2.1.1 Pixel Detectors	4
1.2.1.2 Strip Sensors	4
2 Silicon Detectors	5
2.1 Silicon Sensor Properties	5
2.1.1 PN Junction	6
3 Radiation Damage	11
3.1 Bulk Silicon Damage	11
3.2 Non-Ionizing-Energy-Loss (NIEL) Hypothesis	12
3.3 Characterizing Fluence (Φ_{eq})	14
3.3.1 Leakage Current	14
3.3.2 Effective Doping Concentration N_{eff}	14
3.3.3 Effects of V_{dep} due to Annealing via N_{eff} Analysis	16
3.3.4 PIN Diodes	18
4 Probe Station Experimental Setup	20
4.1 Experimental Setup Overview	20
4.2 Electrical Characterization	21
4.2.1 Capacitance-Voltage Measurement (IV)	22

4.2.2	Current-Voltage Measurement (CV)	22
4.3	Environmental Control	22
4.3.1	Temperature Control	22
4.3.2	Dew-Point / Humidity Control	23
4.4	Test Diodes	23
4.4.1	DZero Diodes	23
4.4.2	PIN Diodes	24
4.4.3	2S and PSS Halfmoon Diodes	24
4.4.4	HGCAL Diodes	25
5	Alibava Station Experimental Setup	27
5.1	2S and PSS Halfmoon Strip Sensors	27
5.2	Radioactive Source	28
5.3	Environmental Control	28
5.4	Measuring Halfmoon Diodes	28
5.4.1	Printed Circuit Board	29
6	Irradiating at RINSC	30
6.1	Rabbit Pneumatic Tube	30
6.2	The Beamport	31
7	Analysis	34
7.1	PIN Analysis	34
7.1.1	Temperature Study	35
7.1.2	Annealing Study	36
7.2	Hamburg Model Analysis	40
7.2.1	Ljubljana Diodes	40
7.2.2	HGCAL Diodes	42
8	Conclusions	51
8.1	RINSC-Ljubljana Cross Calibration	51
8.2	Effects of Concurrent Annealing and Irradiation	52

8.3 Future Work	53
Bibliography	56
Appendix	57

List of Figures

1.1	CERN Complex (from [4])	2
1.2	Integrated particle fluence in $1MeV$ neutron equivalent per cm^2 for the CMS Phase-2 Tracker (from [18])	3
1.3	CMS Detector Diagram (from [13])	3
2.1	Example of doping in Silicon (from [11])	5
2.2	Pn-junction under electrically neutral conditions (from [2])	6
2.3	Typical IV Curve (from [12])	8
2.4	Typical CV Curve (from [12])	9
3.1	Displacement Damage Functions $D(E)$ (from [10])	13
3.2	Fluence Dependence of Leakage Current for Silicon Detectors (from [10])	15
3.3	Current Related Damage Rate α as a Result of Cumulated Annealing Times at Different Temperatures (from [10])	15
3.4	ΔN_{eff} versus cumulative annealing at $60^\circ C$ (from [10])	17
3.5	PIN Fluence Studies at Different Pulsed Currents (from [5])	18
4.1	Picture of the set-up we use for electrically characterizing different silicon diodes at Brown University	20
4.2	Diagram of the sensor and chuck setup in the probe station	21
4.3	(a) The full DZero halfmoon before separating the sensors, (b) Picture of the large diode on the DZero cutout, the top needle is grounded and touching the guard ring pad while the lower needle is touching the bias pad	23
4.4	(a) Halfmoon sensor from Hamamatsu (top left) with other test structures from same wafer, (b) Electrically characterizing the sensors below the strip sensors, a process which is done pre-irradiation as well as twice post-irradiation	25

4.5	Electrically characterizing HGCAL diodes to be used to determine fluence from irradiation runs conducted in the beamport at RINSC	26
5.1	Picture of the halfmoon cut out with strip test structures in the Alibava setup and a strontium source hovering over the strips	27
5.2	(a) Previous way of attaching halfmoon connections to Alibava setup, (b) Printed circuit boards to be used to reliably connect to halfmoon components	29
6.1	Wooden "rabbit" stick with sensors attached,	30
6.2	(a) Example of a kapton layer separating the different sensors of the beamport tube. (b) Hexagonal HGCAL sensor. (c) Beamport tube fully assembled with temperature sensor wires coming out.	32
7.1	Forward voltage (V_f) vs. time for an unirradiated PIN diode	35
7.2	Result of unirradiated PIN-thermometer analysis, found that ramp-up-time would significantly affect cumulative annealing time for short-duration annealing if Annealed on surface not already pre-heated to oven temperature.	36
7.3	Normalized forward voltage (V_f) vs. cumulative annealing time for PIN-diodes for $40^{\circ}C$, $50^{\circ}C$, $60^{\circ}C$ and $70^{\circ}C$	37
7.4	Normalized forward voltage (V_f) vs. cumulative annealing time for PIN-diodes for $80^{\circ}C$, $90^{\circ}C$ and $100^{\circ}C$	38
7.5	Exponential scale factor vs. temperature for PIN diodes	39
7.6	Ljubljana Hamburg analysis of DZero diodes to determine possible transportation annealing en route to Brown University from Slovenia	41
7.7	Hamburg analysis of HGCAL diodes irradiated at RINSC for 43 minutes. (a) HGCAL diode at back of beamport, (b) HGCAL diode at front of beamport, (c) temperature profile from start of irradiation to them being pulled out.	43
7.8	Hamburg analysis of HGCAL diodes irradiated at RINSC for 86 minutes	44
7.9	Hamburg analysis of HGCAL diodes irradiated at RINSC for 216 minutes	45

7.10	Hamburg analysis of HGCAL diodes irradiated at RINSC for 86 minutes	46
7.11	Hamburg analysis of HGCAL diodes irradiated at RINSC for 118 minutes	47
7.12	Hamburg analysis of HGCAL diodes irradiated at RINSC for 43 minutes	48
7.13	Hamburg analysis of HGCAL diodes irradiated at RINSC for 32 minutes	49
8.1	Calculated fluence of PIN and D0 diodes vs. Ljubjana anticipated values	51
8.2	Equivalent cumulative annealing vs. $N_{eff}(t_{min}^{60^{\circ}C})$ for HCGAL diodes irradiated at RINSC	53

List of Tables

7.1	Annealing Fitting Parameters	39
7.2	HGCAL Round 2.2 Extracted Hamburg Values	43
7.3	HGCAL Round 2.3 Extracted Hamburg Values	44
7.4	HGCAL Round 2.5 Extracted Hamburg Values	46
7.5	HGCAL Round 2.6 Extracted Hamburg Values	47
7.6	HGCAL Round 2.7 Extracted Hamburg Values	48
7.7	HGCAL Round 2.8 Extracted Hamburg Values	49

Chapter 1

Introduction

1.1 The Large Hadron Collider

At the Large Hadron Collider, there are four main experimental setups: CMS, LHCb, Atlas and Alice (as seen in figure 1.1). The Compact Muon Solenoid (CMS) is a multipurpose detector and has been primarily focused on observing new signatures of physics such as the Higgs particle or the lightest supersymmetric particles (SUSY). In order to achieve these objectives, as well as other similar ones, the detector needs to be able to precisely measure the four momenta of the muons, electrons, photons and charged particles over a large energy range [3].

The following chapter will serve as a guide to the LHC in general, with special focus to the coming High-Luminosity LHC upgrade and also to the workings of the CMS detector and its silicon sensors which serve as the focus of this thesis.

1.1.1 The High-Luminosity Large Hadron Collider (HL-LHC)

The LHC is the world's largest and most powerful particle accelerator [16]. It was built between 1998 and 2008, when it was first started up. The LHC consists of a 27-kilometer ring of super conducting magnets, in this ring the particles are accelerated to just below the speed of light before they are forced to collide within the designated positions within the detectors. These counter-circulating beams meet with a total collisional energy of 13 TeV at which moment the detectors work to determine the characteristics of the offspring in order to gain insight into the underlying physics which occurred at the moment of collision.

The High-Luminosity LHC (HL-LHC) is a major upgrade of the LHC, the upgrade will allow operators the ability to study these events in more detail by increas-

CERN's Accelerator Complex

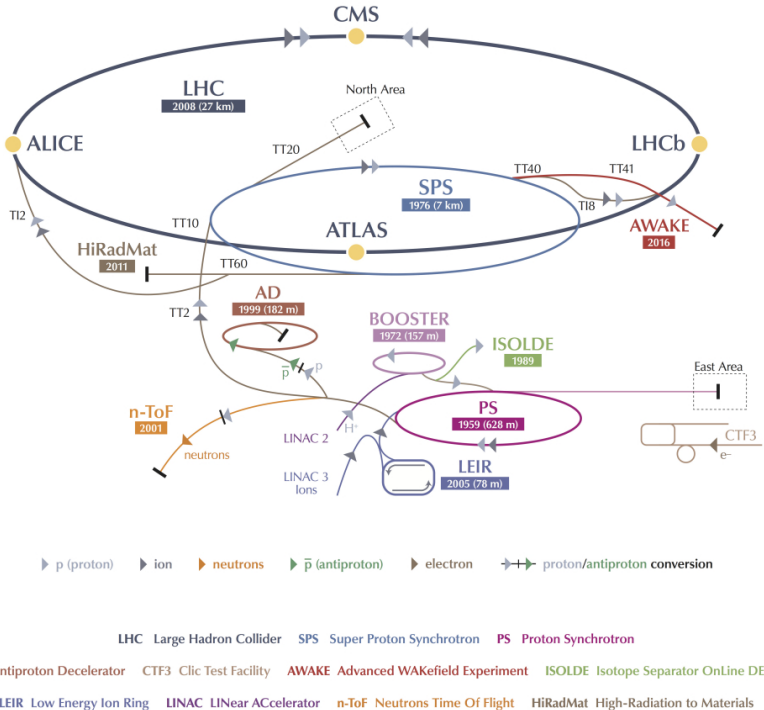


Figure 1.1: CERN Complex (from [4])

ing the number of collisions by a factor of $5 - 7$ from where they were prior to the upgrade [15]. Luminosity is the measure of the number of potential collisions per cross section over a given period of time [15], this quantity integrated is measured in inverse femtobarns [fb^{-1}].

In figure 1.2 we see the integrated particle fluence in 1 MeV neutron equivalent (n_{eq}) per cm^2 , where the estimates in the figure correspond to the total integrated luminosity of $3000 fb^{-1}$ of pp (proton-proton) collisions at $\sqrt{s} = 14$ TeV [18]. Of course not all sections of the CMS detector will see the same amount of fluence over the period of operation for phase-2, in figure 1.3 we can see the different layers of CMS where each of the different types of sensors operate. If we compare the two figures, we'll notice that it is expected that the pixel detector could receive up to $1.0 \cdot 10^{16} MeV n_{eq} cm^{-2}$ while the strip sensors which are housed further from the beam path could receive up to $1.0 \cdot 10^{15} MeV n_{eq} cm^{-2}$ over the course of phase-2 operations. This level of radiation is a concern for any materials, though especially

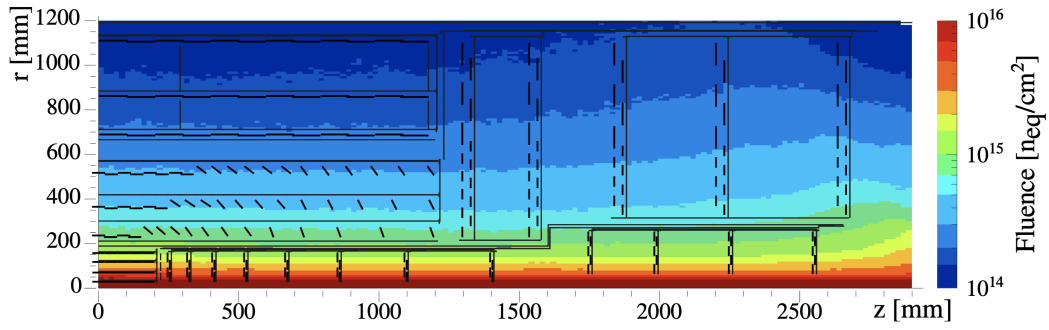


Figure 1.2: Integrated particle fluence in 1MeV neutron equivalent per cm^2 for the CMS Phase-2 Tracker (from [18])

important for the questions of extended accuracy and precision of the silicon particle sensors. This is the reason that there has been extensive research and development of radiation hard materials for the trackers [10].

1.2 The Compact Muon Solenoid Experiment at CERN

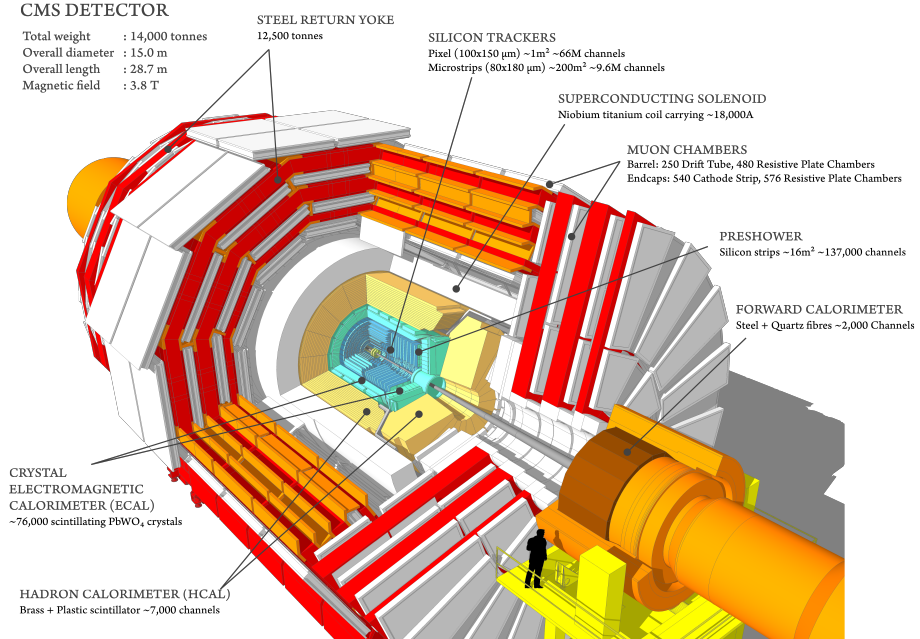


Figure 1.3: CMS Detector Diagram (from [13])

1.2.1 Silicon Sensors

The by-product of the collisions hit the silicon sensors before any of the other detector elements, the reason why they are the first items the particles encounter is because they are used to reconstruct the paths of the particle off-spring with extremely high precision - effectively working as electronic ionization chambers. These paths are then used to determine information about what exactly were the by-products of the collisions. Three designs of silicon sensors are used in the CMS Phase-2 Outer Tracker, all of the types used are n-in-p (highly n-doped strips in p-doped bulk) with p-stop strip isolation [1].

1.2.1.1 Pixel Detectors

The pixel detector contains about 65 million pixels, allowing it to track the paths of particles emerging from the collision with extreme accuracy due to the sensor being able to activate on a very small area as compared to the strip sensor. It is also the closest detector to the beam pipe, with cylindrical layers at 4cm, 7cm and 11cm and disks at either end [14]. Each of the silicon pixel sensors are $100\mu m$ by $150\mu m$, and each of these pixels are connected via bump-wire-bonds to the channels of the readout electronics. The bump-bonds are tiny solder balls have to be put on every cell with relatively high precision [11].

1.2.1.2 Strip Sensors

Directly outside of the region where the silicon pixel detectors are found are the outer tracker modules where two main types are found, the $2S$ and PS modules. The $2S$ modules use two strip sensors with an area of $10^2 cm^2$. Now, the $2S$ sensors are designed with a segmentation along its strips and this results in two rows with 1016 strips with a length of $5cm$ and a pitch of $90\mu m$ [11]. Now, the PS sensors uses a strip ($PS - s$) and a macro-pixel sensor ($PS - p$) with an area of $5 \cdot 10 cm^2$ each.

Chapter 2

Silicon Detectors

The are a number of factors that went into the selection of silicon for the material comprising the particle sensors. Understanding the properties of semiconductor sensors and silicon in general is crucial for the later work that follows, this chapter will serve to briefly summarize some of the main features.

2.1 Silicon Sensor Properties

Silicon has four valence electrons, and when it's in crystalline form all four valence electrons are shared in covalent bonds with neighbouring silicon atoms. In order to make the transportation of electrons easier within the lattice of the silicon it is common practice to change the electrical properties of a semiconductor by adding (doping) different elements into the structure of the silicon crystal lattice. There are two types of dopants, the first type adds one additional electron to the lattice region due to their being five valence electrons on the dopant atom. This type of silicon is labeled n-doped and the concentration of donors is typically N_D , typically phosphorous is used as the donor atom.

The second type adds a positive "hole", the hole is created when the dopant has

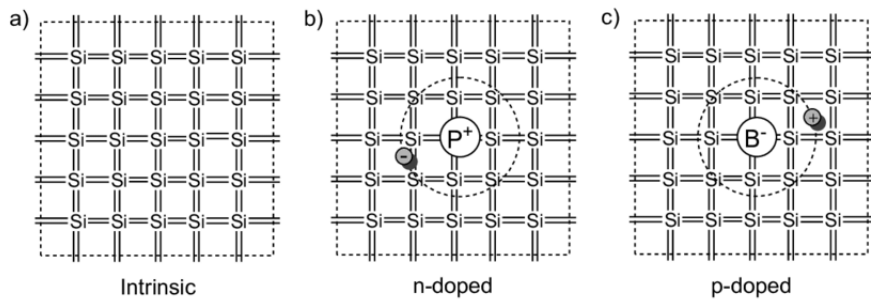


Figure 2.1: Example of doping in Silicon (from [11])

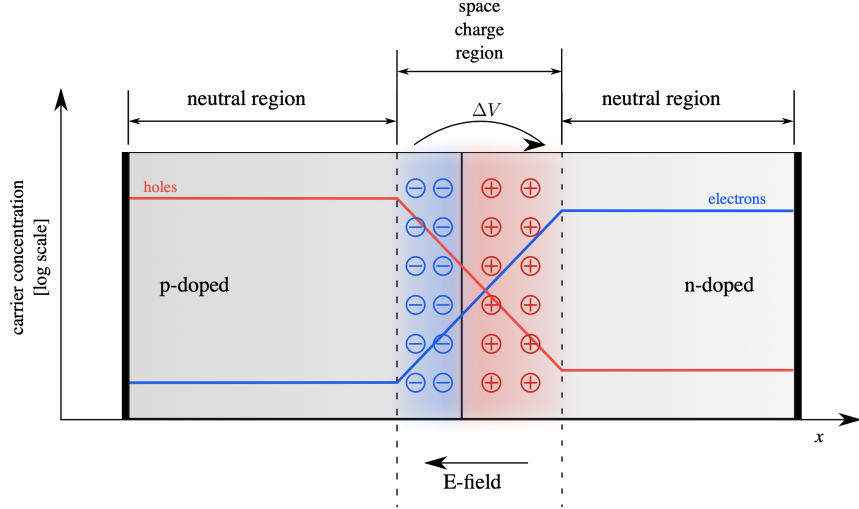


Figure 2.2: Pn-junction under electrically neutral conditions (from [2])

only three valence electrons, and so the region surrounding the dopant is effectively missing one electron. This type of silicon is called p-doped and typically boron or aluminum is used. The concentration of acceptors is labelled N_A .

In figure 2.1 we can see a pictorial representation of the different silicon types (a) shows Intrinsic silicon, (b) shows a n-type Si with donor (phosphorus). Finally in (c) we see a p-type Si with acceptor (boron). Typical values for the doping concentration range between 10^{12} cm^{-3} and 10^{18} cm^{-3} [8].

2.1.1 PN Junction

In figure 2.2 we see the simplest pn-device which is referred to as a pn-junction. The p-doped and n-doped layers of a diode are sandwiched by two parallel metal electrodes. The configuration is comparable to a plate capacitor. Thus, the capacitance of a diode is given by the permittivity of Silicon ϵ_{Si} (where $\epsilon_{Si} = \epsilon_0 \cdot \kappa_{Si}$ and ϵ_0 is the permittivity of free space), the area of the diode A and the width of the depletion zone w seen in equation 2.1:

$$C = \epsilon_{Si} \frac{A}{w} \quad (2.1)$$

A positive terminal connected to the p-doped region and a negative terminal connected to the n-doped region will affect the space charge region of the pn-junction

by reducing the electric field and thus reducing the width of the depletion region. This is known as forward biasing, while connecting the terminals the other way around is simply called reverse biasing.

Applying a bias voltage V in the reverse direction to the sensor, the region of ionized acceptors and donors is named the space-charge-region (which can be seen in figure 2.2) and the effective potential is

$$V + V_{bi} = \frac{1}{e} (E_i^p + E_i^n) = \frac{k_B T}{e} \ln \left(\frac{N_A N_D}{n_i^2} \right) \quad (2.2)$$

Now, the thickness of the space charge region is $w = d_p + d_n$ and can be given as (calculation found in [6])

$$w(V) = \sqrt{\frac{2\epsilon_{Si}}{e} \left(\frac{1}{N_A} + \frac{1}{N_D} \right) (V + V_{bi})} \quad (2.3)$$

where V_{bi} is the so-called built-in-voltage, N_A is the concentration of acceptor atoms, N_D is likewise the concentration of donor atoms and ϵ_{Si} is the permittivity of silicon where $\epsilon_{Si}/\epsilon_0 \approx 11.8$. Typically V_{bi} is usually insignificant compared to the bias applied to the sensors so we can approximate the depletion region as

$$w(V) \approx \sqrt{\frac{2V\epsilon_{Si}}{eN_D}} \quad (2.4)$$

Now, in order to utilize the entire piece of silicon for detecting particles we need to expand this depletion region over throughout the entire thickness of the silicon detector. The voltage at which this is achieved is called the depletion voltage (V_{dep}) and is given by

$$V_{dep} = \frac{eN_D d^2}{2\epsilon_{Si}} \quad (2.5)$$

In a reverse bias situation the leakage current versus applied voltage follows a characteristic pattern (as seen in figure 2.3). The breakdown is defined as the rapid increase of the current when the reverse bias goes above a certain limit (V_{BD}).

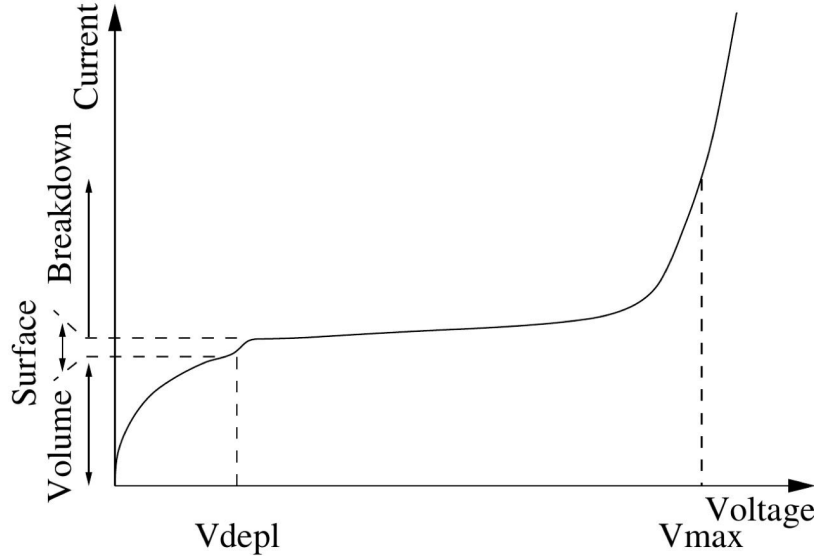


Figure 2.3: Typical IV Curve (from [12])

Now in the case of measuring the capacitance we can refer to the following equation

$$w(V) = \sqrt{\frac{2\epsilon_{Si}}{e} \left(\frac{1}{N_A} + \frac{1}{N_D} \right) (V + V_{bi})} \quad (2.6)$$

where the built-in voltage V_{bi} can be neglected because $V \gg V_{bi}$ is assumed, which is the case in the operation of silicon detectors. The important thing to note is that the depleted region increases linearly with the square root of the bias

Now one could then use eqn. 2.6 and substitute it into eqn. 2.1 to arrive at the following conclusion

$$C = \epsilon_{Si} A N_A N_D \sqrt{\frac{e}{2\epsilon_{Si} (N_A + N_D) (V + V_{bi})}} \quad (2.7)$$

We can see that the capacitance will decrease proportionally with the square root of the bias voltage until the region of depletion extends over the entire volume of the diode. At voltages higher than the depletion voltage we see a constant capacitance where the value of the capacitance for this regime corresponds to the geometrical capacitance of the diode when considered as a parallel plate capacitor. The value of the capacitance for that situation is:

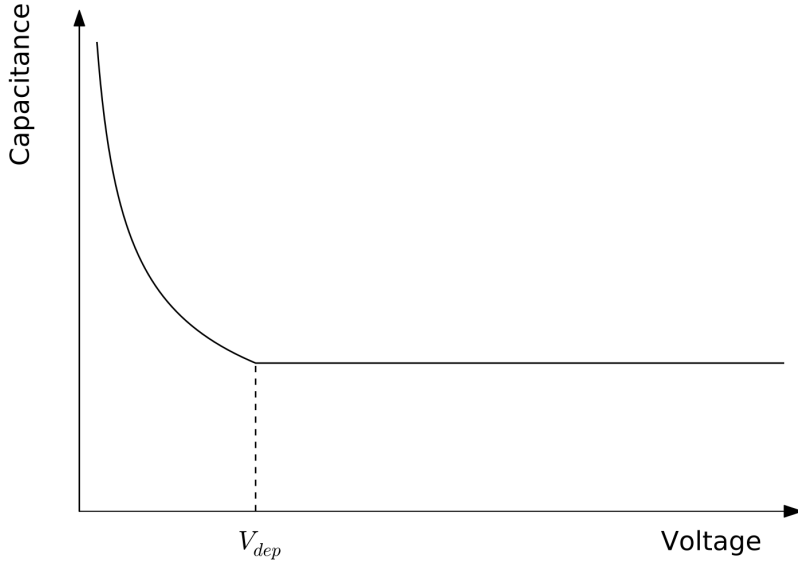


Figure 2.4: Typical CV Curve (from [12])

$$C = \epsilon_{Si} \frac{A}{d} \quad (2.8)$$

where d is simply the total thickness of the diode. Additionally, one can express the reverse current dependence on the temperature by

$$I \propto T^2 \cdot e^{-\frac{E_g}{2k_B T}} \quad (2.9)$$

where E_g is the energy gap of the silicon being biased. In our own research we found it very useful to be able to convert between leakage currents at one temperature and leakage currents at another temperature, we did that using the following formula

$$I(T) = I_{tot} \cdot \left(\frac{T}{T_0} \right)^2 \cdot e^{-\frac{E_g}{2k_B} \left(\frac{1}{T_0} - \frac{1}{T} \right)} \quad (2.10)$$

where I_{tot} is the measured leakage current at T_0 , T is the temperature, E_g is the band gap energy of silicon and k_B is of course the Boltzmann constant. Now, as we will cover in the following chapter, as silicon is damaged by radiation the leakage current per unit volume ΔI increases linearly with fluence Φ_{eq} [10], the slope of this

linear relationship is called the current related damage constant (α) and can be seen in the following equation

$$\Delta I = \alpha \Phi_{eq} V \quad (2.11)$$

where V is the volume of the silicon sensor.

Chapter 3

Radiation Damage

Generally speaking, in high energy physics (HEP) experiments, the aim of the silicon tracking detectors is the detection of particles passing through the device which makes use of the radiation-matter interactions. Although as one can imagine, the very nature of these interactions can significantly alter the nature of the detector when these kinds of interactions are numerous and over a long period of time. Of course this is of large concern for the HL-LHC upgrade, and so fully characterizing the effects is of great importance. Permanent radiation damage can manifest in two predominate ways, those ways being bulk and surface damage. Though it is the bulk damage which is typically the limiting factor for the use of silicon detectors in HEP experiments, so it is this regime the chapter will primarily focus on. Further reading on both surface and bulk damage can be found in the PhD Thesis by Michael Moll [10].

The following chapter will cover radiation damage mechanisms, characterizations of those changes, and the behavior of those changes with respect to temperature after irradiation.

3.1 Bulk Silicon Damage

Silicon bulk damage is due primarily to impinging particles hitting silicon atoms out of their original place in the crystal lattice. When an incoming particle first hits a silicon atom in the crystal lattice it is called a "primary knock-on atom" (PKA). The PKA then leaves its original lattice site which results in a silicon interstitial and a vacancy where the atom originally was (Frenkel Pair). What Van Lint found was that the primary recoil atom could only be displaced if the energy imparted by the oncoming particle was more than some displacement threshold energy $E_d \approx 25eV$

[17]. One could make a simple non-relativistic calculation for the energy that could be transmitted via elastic scattering; if the mass of the incident particle is $m_{incident}$ with kinetic energy $E_{incident}$ then the maximum energy that could be imparted into the silicon atom in the lattice is

$$E_R = 4 \cdot E_{incident} \cdot \frac{m_{incident} \cdot m_{Si}}{(m_{incident} + m_{Si})^2} \quad (3.1)$$

From the above equation and the displacement threshold energy one could calculate the necessary kinetic energy of the incident particle necessary to displace a silicon atom from the lattice, though this is not something I will do here. Refer to [17] and [10] for more information on the subject.

3.2 Non-Ionizing-Energy-Loss (NIEL) Hypothesis

When considering the particles incident on the silicon detectors, its not the lighter-mass charged hadrons we need to worry about too much - this is because they interact primarily by the coulomb interaction and so most of these interactions only lead to ionization. What needs to be considered however are the neutrally charged neutrons which only interact with the nucleus of the silicon atoms. Most of the interactions between neutrons and the silicon nuclei can be modeled as elastic collisions, though at energies above 1.8MeV nuclear reactions can also take place [17].

Now that we know who our likely bulk damaging culprits are (high energy neutrons), we need a way to model how radiation damage scales with particle energy. The model which we use is called the Non-Ionizing-Energy-Loss-Hypothesis, or NEIL hypothesis. The simplifying assumption of the NEIL hypothesis is that the change in the material due to displacement damage scales linearly with the energy of the incident particles, this doesn't account for any spatial considerations of the incident particles or damage due to PKA cascades. In order to arrive at a calculation for the NEIL, one can use the Lindhard-Partition-Function $P(E_R)$ [6] and then the NEIL can be expressed by the displacement-damage-cross-section

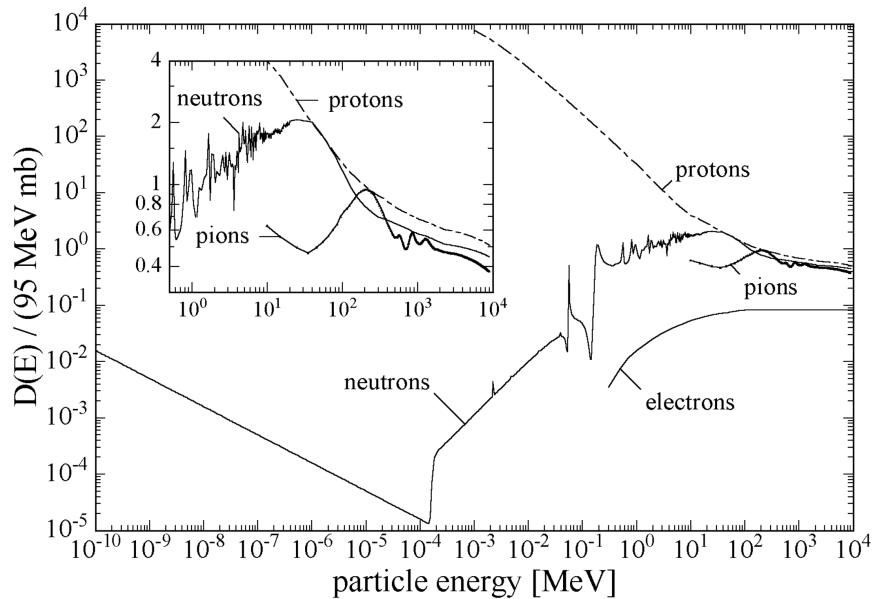


Figure 3.1: Displacement Damage Functions $D(E)$ (from [10])

$$D(E) := \sum_{\nu} \sigma_{\nu}(E) \cdot \int_0^{E_R} f_{\nu}(E, E_R) P(E_R) dE_R \quad (3.2)$$

where ν indicates all possible interactions between the incident particle of energy E and the silicon atoms in the crystal leading to displacement in the lattice. σ_{ν} is the cross section corresponding to the reaction, $f_{\nu}(E, E_R)$ is the probability density function for the generation of a PKA with recoil energy E_R by a particle with energy E . This is then integrated over all recoil energies, where a recoil energy less than the threshold displacement energy ($P(E_R < E_d) = 0$) are identically zero [10]. From this function one can relate experimental fluence and equivalent fluence to one another using a linear relationship: $\Phi_{eq} = \kappa \Phi_{exp}$. The constant κ is called the "hardness factor", and is defined to be identically one for 1 MeV neutrons. The purpose of this is that different experimenters will still be able to compare data taken from samples irradiated by particles at different energies.

3.3 Characterizing Fluence (Φ_{eq})

When developing radiation hard silicon detectors it is important to evaluate the amount of radiation damage that has taken place and how those effects might be reversed. The following sections will serve to illustrate the different approaches we have made in determining the amount of fluence the irradiated silicon sensors have experienced and also how we characterized the temperature effects to the radiation damage. The two main ways we use to characterize the fluence were changes in the leakage current (which scales linearly with the fluence) and the changes to the depletion voltage (which also scaled with the fluence).

3.3.1 Leakage Current

Leakage current is any current which is flowing through a reverse biased pn junction. When the sensor is not irradiated, the leakage current is due primarily to two different processes. The first process being the charge carriers within the doped silicon crossing the junction which is called "diffusion current", and the second cause from the generation of charge carriers in the depletion zone, called "generation current". Experimentally it has been shown that leakage current scales linearly with fluence according to equation 3.3.

$$\alpha\Phi_{eq} = \frac{\Delta I}{V} \quad (3.3)$$

Where in our fluence analysis we are using a value of $\alpha = (3.99 \pm 0.03) \cdot 10^{-17} A/cm$ which we used from the work of R. Wunstorf [20] which was later confirmed by M. Moll [9] to work well for annealing values of 80 min at 60C. In figure 3.2 we can see how well this linear relationship holds for a wide range of parameters.

3.3.2 Effective Doping Concentration N_{eff}

The effective doping concentration is simply the difference between the concentrations of the ionized donors and acceptors within the depletion zone. If one wanted

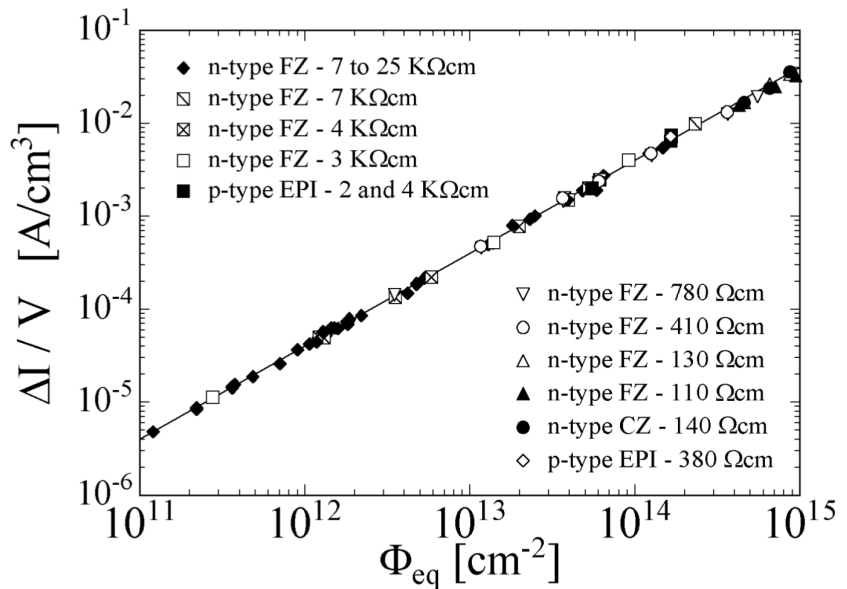


Figure 3.2: Fluence Dependence of Leakage Current for Silicon Detectors (from [10])

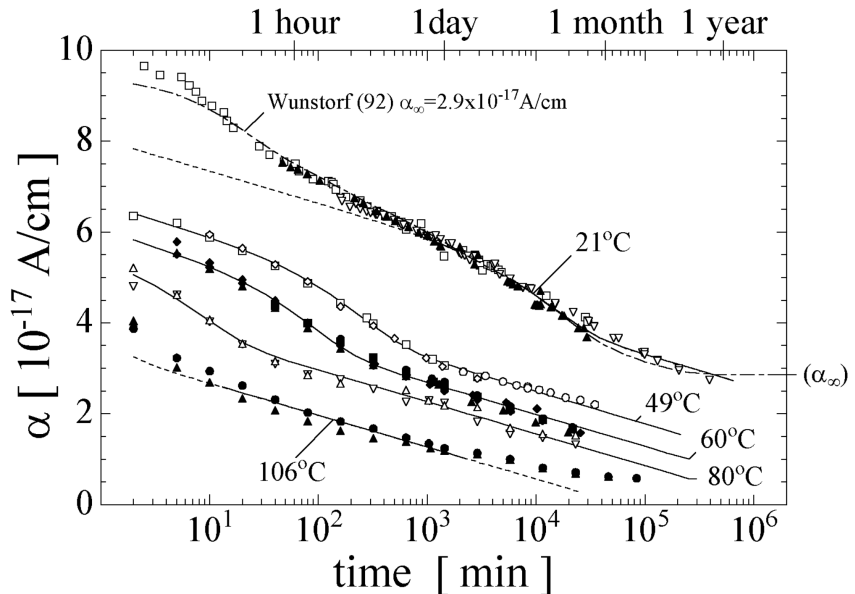


Figure 3.3: Current Related Damage Rate α as a Result of Cumulated Annealing Times at Different Temperatures (from [10])

to, one could derive the width of the depletion zone as a function of applied voltage and N_{eff} using Poissons equation, something which will not be presented here. That solution is equation 2.6, although written in only a slightly different way below in equation 3.4

$$w(V) = \sqrt{\frac{2\epsilon_0\epsilon_{Si}}{e|N_{eff}|}(V + V_{bi})} \quad (3.4)$$

Now, as we mentioned in the previous chapter we expect that $V \gg V_{bi}$, if we then also have $V = V_{dep}$ we will arrive at the following equation

$$|N_{eff}| = \frac{2\epsilon_0\epsilon_{Si}}{ed^2}|V_{dep}| \quad (3.5)$$

where d is the width of the diode in question. The following section will aim the answer how N_{eff} and V_{dep} are affected by temperature, and what we will find is that there is a combination of temperature and time which will reverse some of the detrimental affects due to radiation damage.

3.3.3 Effects of V_{dep} due to Annealing via N_{eff} Analysis

V_{dep} shows a very different response to annealing than the leakage current, and that difference can be seen in the change to N_{eff} which is after all proportional to V_{dep} . The change in N_{eff} is described by the Hamburg Model and was given the following parameterization due to M. Moll [10] in his 1999 thesis.

$$\Delta N_{eff}(\Phi_{eq}, t) = N_C(\Phi_{eq}) + N_A(\Phi_{eq}, t) + N_Y(\Phi_{eq}, t) \quad (3.6)$$

where the term $N_C(\Phi_{eq})$ is called the stable damage and is given by the equation below

$$N_C(\Phi_{eq}) = r_C N_{eff,0} \left(1 - e^{-C\Phi_{eq}}\right) + g_c \Phi_{eq} \quad (3.7)$$

more information about each of the terms can be found in the 2006 dissertation by Fugeri [3], and we eventually want to get to a fully described equation for $\Delta N_{eff}(\Phi_{eq}, t)$ which will be used for determining differences in our irradiation procedures for the HL-LHC silicon sensor test structures. The other terms in equation 3.6 I will list quickly.

$$N_A(\Phi_{eq}, t) = \Phi_{eq} \sum_i g_{a,i} e^{\frac{t}{\tau_{a,i}}} \quad (3.8)$$

Equation 3.8 is for $N_A(\Phi_{eq}, t)$ and is called the beneficial annealing which is the sum of exponential decays of radiation induced damage. Typically these exponential decays can be summarized into one exponential damage decay with a time constant τ_a using a Arrhenius relation, this is the assumption we will make. The last term in 3.6 to speak about is $N_Y(\Phi_{eq}, t)$ which is called the reverse annealing term.

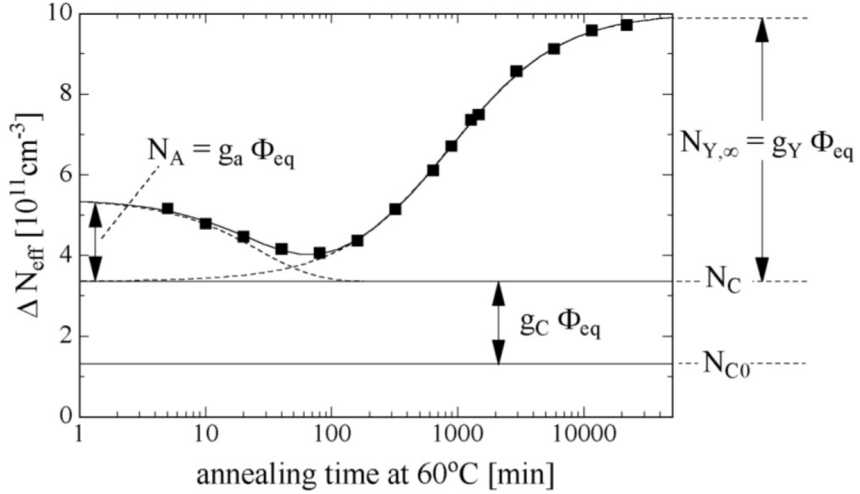


Figure 3.4: ΔN_{eff} versus cumulative annealing at $60^\circ C$ (from [10])

$$N_Y(\Phi_{eq}, t) = g_Y \Phi_{eq} \left(1 - \frac{1}{1 + \frac{t}{\tau_y}} \right) \quad (3.9)$$

Where in equation 3.9 $g_Y = (5.16 \pm 0.09) \cdot 10^{-2} \text{ cm}^{-1}$ and the time constant τ_y can be expressed using an Arrhenius plot as was done for the beneficial annealing time constant term from equation 3.8.

$$\Delta N_{eff}(t) = g_a e^{-\frac{t}{\tau_a}} \Phi_{eq} + g_y \left(1 - \frac{1}{1 + \frac{t}{\tau_y}} \right) \Phi_{eq} + r_C N_{eff,0} \left(1 - e^{-C \Phi_{eq}} \right) + g_c \Phi_{eq} \quad (3.10)$$

where $\Delta N_{eff}(t) = N_{eff}(t_{ann}) - N_{eff,pre-irr}$ and g_a is called the beneficial annealing introduction rate, g_y is the reverse annealing introduction rate, τ_a is the beneficial

annealing time constant, τ_y is the reverse annealing time constant and Φ_{eq} is of course the equivalent fluence.

Further reading of anticipated parameter values and their significance can be found in [10] and [3]. A typical graph for the effective doping concentration can be seen in figure 3.4, we notice that there is a minimum in ΔN_{eff}

3.3.4 PIN Diodes

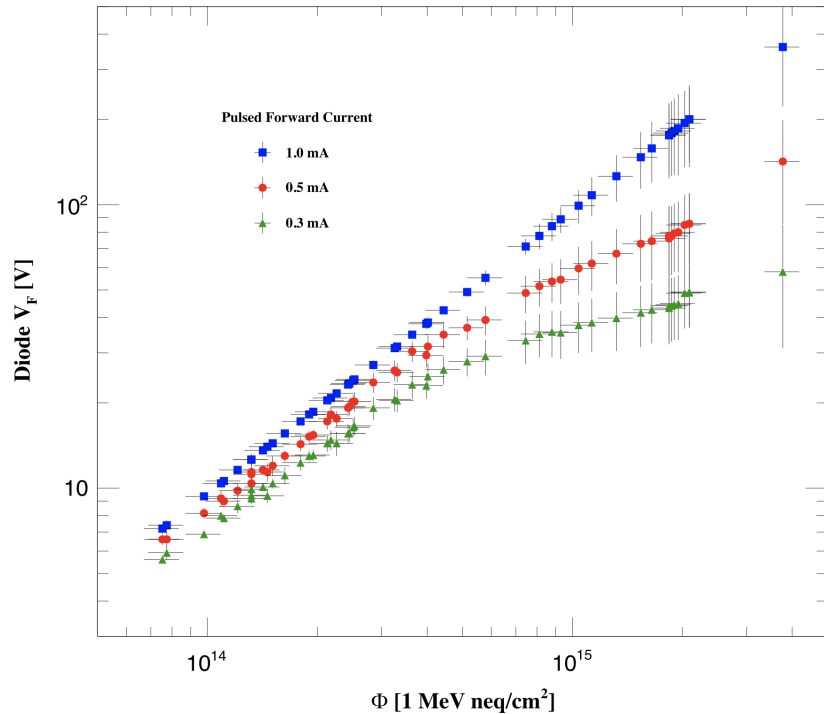


Figure 3.5: PIN Fluence Studies at Different Pulsed Currents (from [5])

In Figure 3.5 from the paper by Hoeferkamp et al. [5], we see diode forward voltage as a function of applied fluence, for three choices of applied current amplitude. The vertical error bars indicate the combined uncertainties related to temperature variation during the irradiation process, current pulse width, and sourcemeter precision. The horizontal error bars indicate the uncertainty deriving from counting statistics on calibration foils in the gamma spectrometer.

Based on the linear fit of Figure 3.5, Hoeferkamp et al. showed a good relation

between diode forward voltage and fluence, where the forward voltage was measured after applying a $1mA$ for approximately .38s. That relation is seen in Equation 3.11.

$$\Phi_{neq} = 1.1 \cdot 10^{13} \cdot V_f - 6.2 \cdot 10^{10} \quad (3.11)$$

Chapter 4

Probe Station Experimental Setup



Figure 4.1: Picture of the set-up we use for electrically characterizing different silicon diodes at Brown University

All of the test structures which we electrically characterized were done so on the probe station (pictured in figure 4.1). We call it the probe station because we are able "probe" a sensor using needles (example seen in figure 4.3) on a precise spot, these needles are then connected to different instruments depending on what we're interested in measuring.

4.1 Experimental Setup Overview

We measured n and p-type sensors, irradiated and non-irradiated sensors and at a range of temperatures from $+20^{\circ}C$ to $-20^{\circ}C$. The specific names of the sensors include DZero diodes, 2S and PSS halfmoon diodes, HGCAL diodes and also PIN diodes. For all but the PIN diodes, the sensors were placed in a climate controlled box on an aluminum chuck. The sensor is made to "stick" to the chuck using a

vacuum pump pulling air from small holes on the chuck. If the temperature we are aiming to measure the sensor is below the dewpoint in the box, we can flush the box with nitrogen from an adjacent nitrogen bottle - otherwise we pass air into the box through desiccants to ensure the box is dry.

4.2 Electrical Characterization

The diodes are biased by applying voltage to the entire aluminum chuck by using a Keithley 237 High Voltage Measurement Unit ($\pm 1100V$). This same instrument is then used to measure the total current it sources which is the sum of the guard and bias ring currents. For diodes which have a guard ring a needle is placed on the pad to ground in order to reduce fringe fields near the bulk material. The bias ring current is measured using a Keithley 6485 Picoammeter using a probe needle, both needles used at the probe station have a tip width of about $7\mu m$.

All of the instruments are controlled by LabView via GPIB, where we can specify parameters like voltage step size, number of measurements taken, whether it is a negative or positive bias and also maximum voltage. Typically, but not always, at each voltage step the measurement is made four independent times half a second apart and an average of those four measurements is quoted.

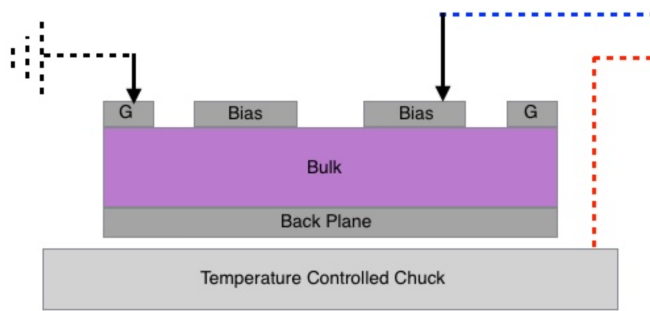


Figure 4.2: Diagram of the sensor and chuck setup in the probe station

4.2.1 Capacitance-Voltage Measurement (IV)

When doing a CV measurement we first ground guard ring and then pass the red and blue lines of figure 4.2 through an isolation box and then to a HP 4284A LCR Meter which takes the CV measurement. The isolation box helps ensure that the LCR meter doesn't receive voltages which might fry it. Once the signal is received by the LCR meter, the LCR meter will output an AC voltage signal into the circuit at typically two different frequencies ($1KHz$ and $10KHz$) where then the LCR will measure the response to determine the capacitance of the diode.

4.2.2 Current-Voltage Measurement (CV)

When taking an IV measurement, as described briefly above in section 4.2, one needle is placed on the guard ring and another is placed on the bias ring pad (diagram of this situation is seen in figure 4.2). The red line is connected to the Keithley

4.3 Environmental Control

In order to make the measurements made consistently, the probe station has environmental controls which allow for the fine-tuning of a number of parameters relevant to the measurement taking process.

4.3.1 Temperature Control

The current of the diodes being measured is highly temperature dependent, for that reason we require that once a temperature has been set that there be no more than a $\pm 0.05^{\circ}C$ deviation from that temperature. To achieve this result two devices are used, the first is a Julabo FP89-HL Ultra-Low Refrigerated Circulator flows coolant just below the chuck to within a degree or two of the set temperature. The second device employed is a peltier thermoelectric cooler, which cools by using the Peltier effect to create a heat flux at the junction of two different types of materials. This allows for the fine temperature control, where the voltage of the peliter is controlled

using a proportional–integral–derivative (PID) controller. All diode measurements made on the probe station kept temperature variations well within $\pm 0.05^\circ C$.

4.3.2 Dew-Point / Humidity Control

One of the more crucial aspects to measuring silicon diodes at low temperatures is ensuring no condensation accumulates on the surface of the diodes when measuring them. To ensure a dry measuring environment we pass compressed air through desiccant, and if this is not dry enough we use a N_2 bottle during measuring. We monitor the dewpoint in real time via an instrument inside of the measurement box, and generally try and make sure that the dew point is at least $1.5^\circ C$ below the temperature we are measuring at.

4.4 Test Diodes

Below I will describe the diodes measured on the probe station. Unirradiated diodes are measured at $+20^\circ C$, irradiated but pre-annealed diodes are measured at $0^\circ C$ and irradiated and annealed diodes measured at $-20^\circ C$.

4.4.1 DZero Diodes

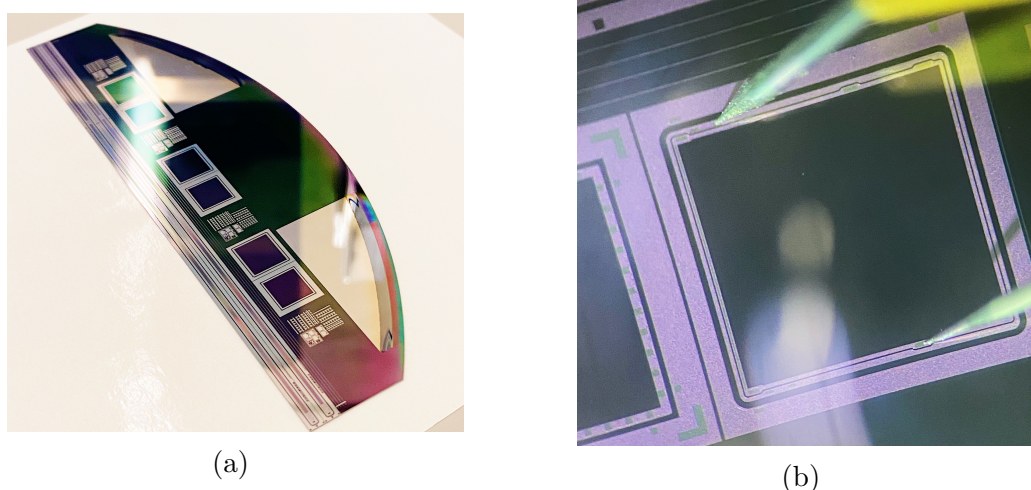


Figure 4.3: (a) The full DZero halfmoon before separating the sensors, (b) Picture of the large diode on the DZero cutout, the top needle is grounded and touching the guard ring pad while the lower needle is touching the bias pad

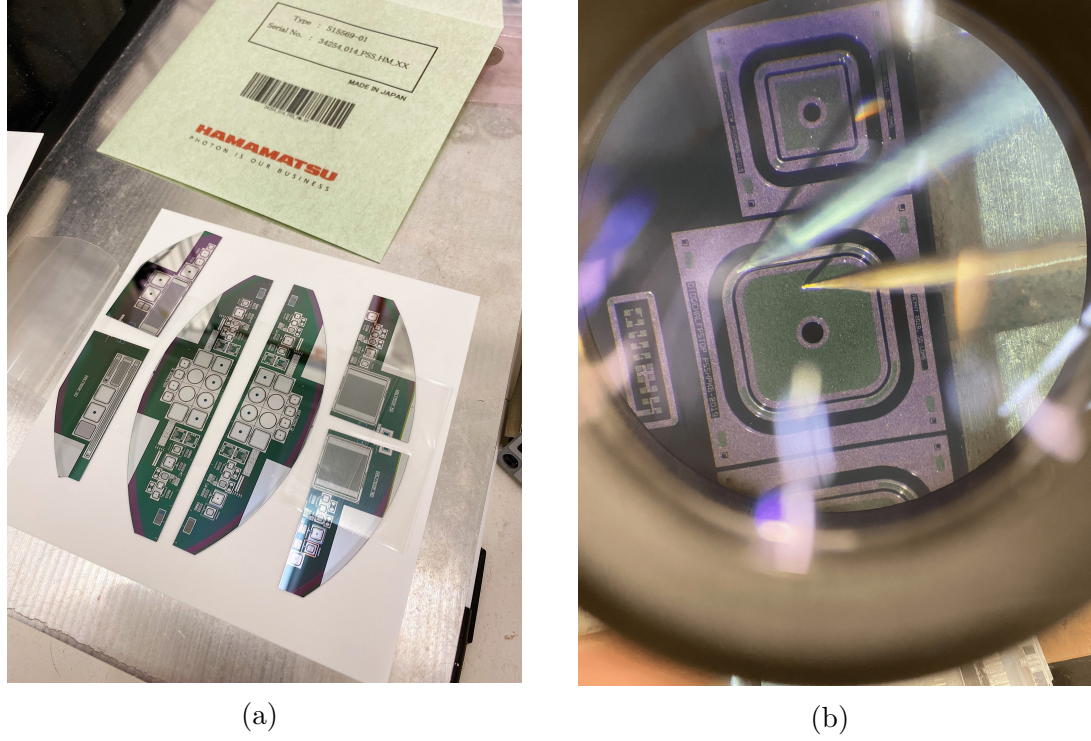
The predominantly measured diode at the probe station is the D0 diodes from an old FermiLab experiment. A picture of the halfmoon we break the diodes away from is shown in figure 4.3 (a), in (b) is a picture of the large diode on the probe station chuck with one needle on the bias pad and the other needle on the guard ring pad. There are in-fact two diodes on each DZero cutout, though we only utilize the larger of the two because it is the only one with a guard ring surrounding the diode's bulk material. We use these diodes in beamport runs (to be described in section 6.2) and in the rabbit irradiation's (to be described in section 6.1). After irradiation, when calculating the fluence using equation 3.3, we use take the volume to be $V = 0.010846\text{cm}^3$ for the large diode (the only one we use for measurements) where the thickness of the diode is $d = 290\mu\text{m}$.

4.4.2 PIN Diodes

A PIN diode is a diode with a small, undoped intrinsic semiconductor region between a p-type semiconductor and an n-type semiconductor region. Their accuracy with fluence measurements is limited, so we use them primarily in rabbit fluence runs to estimate longitudinal and face-to-face fluence values. The method by which we measure fluence is described in section 3.3.4

4.4.3 2S and PSS Halfmoon Diodes

The 2S and PSS halfmoon diodes (seen in figure 4.4) we measure on the probe station are small test structures from the same silicon wafers used for the full-scale sensors to be used at CMS. The irradiation studies we perform on them are analyzed on both the probe and Alibava stations. The probe station we use for electrically characterizing diodes like those seen in figure 4.4 (b), while at the Alibava station we are testing the miniature strip sensors directly below the diodes. That station uses a radioactive source (strontium-90) to see how well the strips collect charge after irradiation at different fluences. Further information about that process will be described in chapter 5.



(a)

(b)

Figure 4.4: (a) Halfmoon sensor from Hamamatsu (top left) with other test structures from same wafer, (b) Electrically characterizing the sensors below the strip sensors, a process which is done pre-irradiation as well as twice post-irradiation

4.4.4 HGCAL Diodes

The final test structures to speak about are the HGCAL diodes, these we recently started measuring (only at the end of 2021) and we're measuring them to understand the fluence received by HGCAL prototype sensors which we irradiated with neutrons. One big advantage of the HGCAL diodes is that they have a thinner bulk which allows us to determine the depletion voltage at higher fluences. The other advantage is they have a larger bias pad (being almost the entire area of the diode) and much larger guard ring pads. There are three diodes which are present on these cutouts, they are called DIODE, DIODEHALF and DIODEQUARTER. The volumes we use for fluence calculations are; $V_{DIODE} = 3.114 \cdot 10^{-3} \cdot cm^3$, $V_{DIODEHALF} = 7.559 \cdot 10^{-4} \cdot cm^3$ and $V_{DIODEQUARTER} = 1.954 \cdot 10^{-4} \cdot cm^3$. The values for the volumes were provided to us by the HGCAL group, and confirmed using a Smart Scope.

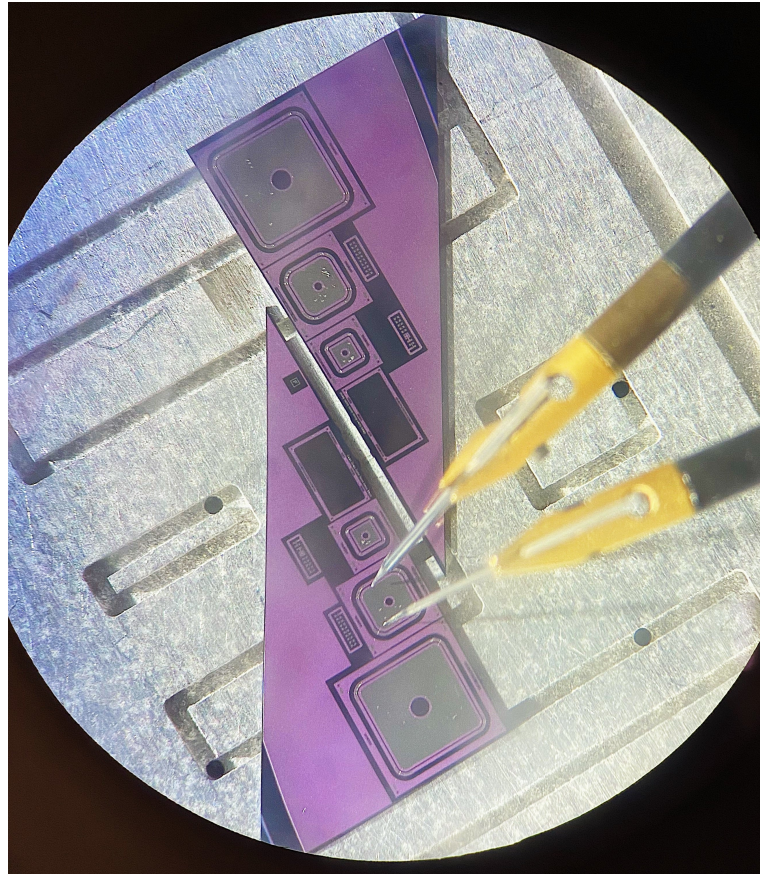


Figure 4.5: Electrically characterizing HGCAL diodes to be used to determine fluence from irradiation runs conducted in the beamport at RINSC

Chapter 5

Alibava Station Experimental Setup

5.1 2S and PSS Halfmoon Strip Sensors

The test diodes we are using on the Alibava station are those which have small strip test structures. On each of the 2S and PSS silicon wafers are these test structures (seen in figure 4.4). Both the 2S and PSS are p-type silicon sensors.

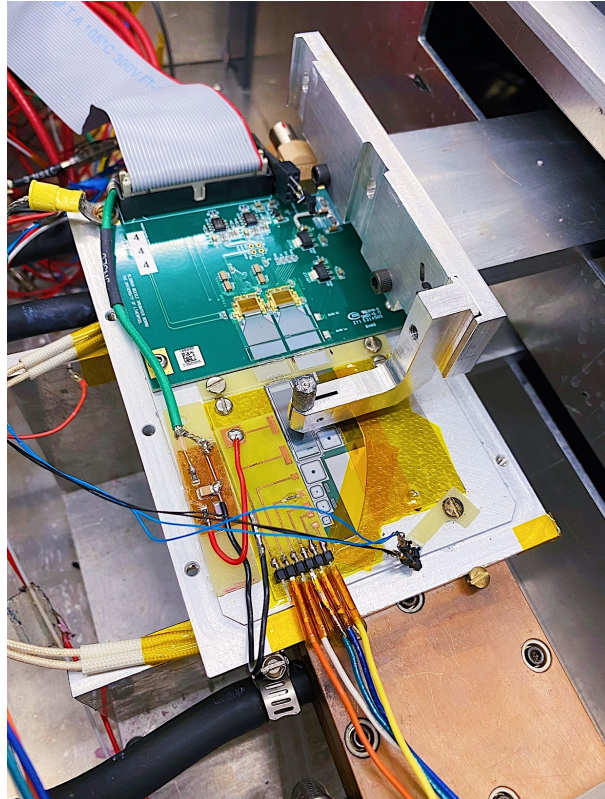


Figure 5.1: Picture of the halfmoon cut out with strip test structures in the Alibava setup and a strontium source hovering over the strips

5.2 Radioactive Source

As seen in the middle of the image in figure 5.1 we can see a small silver cylinder hovering above the silicon strip sensor of the halfmoon, this is the radioactive source (Strontium-90) which we use to test the combination of effects of annealing and irradiation.

5.3 Environmental Control

The exact same kinds of considerations with respect to temperature control are taken at the Alibava station as they were at the probe station. Differences are only in the rate at which temperature measurements are made and altered. Refer to section 4.3 for more information.

5.4 Measuring Halfmoon Diodes

The measuring process for both sensors is the same, initially when the sensors are received we measure the diodes and strips to ensure that the sensors are in good working order. Then they are irradiated at RINSC in a rabbit tube (to be further described in section 6.1), and upon being returned to Brown the halfmoon sensors are initially annealed for a 20 minute period at $60^{\circ}C$. After the initial annealing the strips are bonded to an Alibava system which is able to measure the collected charge in one or two microstrip silicon sensors by reading out all the channels of the silicon strip sensor (see [7] for further discussion). After bonding we measure the readout of the collected charge on the strips at regular annealing steps and at different bias voltages. From this we are able to determine how the collected charge on the strips is affected by different irradiation doses and how that is further affected by annealing for increasing time periods. Further discussion on those results and processes will not be discussed in this thesis, though more reading on the results of annealing on collected charge on p-type strip sensors can be found in [19].

5.4.1 Printed Circuit Board

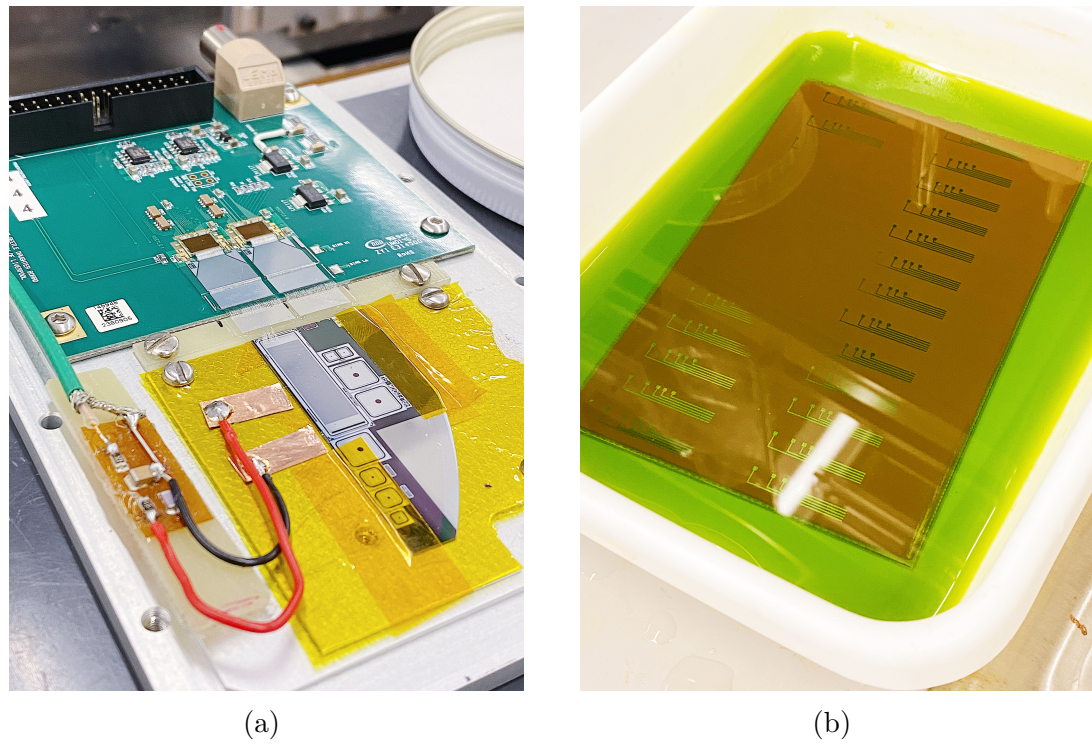


Figure 5.2: (a) Previous way of attaching halfmoon connections to Alibava setup, (b) Printed circuit boards to be used to reliably connect to halfmoon components

Initially we were applying the bias and ground to the sensor using the configuration seen in figure 5.2 (a), and then measuring the diodes on the probe station using the probe needle but this turned out to be time intensive and the copper tape we were using for bonding pads was not reliable. We decided to make a printed circuit board (seen in figure 5.2 (b) with the completed result in figure 5.1). This turned out as expected, with easier bonds and quicker measurement procedure. The schematics for the PCB can be found in section 8.3.

Chapter 6

Irradiating at RINSC

When irradiating at The State of Rhode Island Nuclear Science Center (RINSC), we have several delivery methods at our disposal. Both have pros and cons associated with each one, which I will briefly describe below.

6.1 Rabbit Pneumatic Tube



Figure 6.1: Wooden "rabbit" stick with sensors attached,

Seen in figure 6.1 is a wooden stick with different sensors and attachments all held together with kapton tape. Directly in the center is a PSS halfmoon sensor which has already been initially measured, also on that same face are two PIN sensors. We use the PIN sensors for fluence estimations along each face (because there are slight

variations across a single face due to the orientation of the rabbit within the tube near the center of the reactor). In addition we also use the fluence values from each of the PIN diodes to better estimate the likely orientation of the rabbit stick during irradiation (which side was pointing up etc.). Orientation is important to know because when the pneumatic tube is sent into the reactor the exact neutron fluence it receives depends on its orientation with respect to the core.

One of the benefits of the rabbit irradiation method over the beamport is that it allows for a shorter exposure time to the reactor, this is because once the time within the reactor is achieved the pneumatic tube can simply call the rabbit back where as in the beamport the process is more complex. A shorter time in the reactor allows greater consistency in fluences across different runs. Unfortunately though, due to the nature of how the rabbit stick is sent into the reactor it is not possible to precisely monitor the temperature within the rabbit stick. The only estimates of the temperature we are able to get are rough estimates on the maximum temperature with stickers we apply to the face of the rabbit. For this reason it is difficult to assess the effect of concurrent annealing during irradiation which is important for longer irradiation (higher fluence) runs.

6.2 The Beamport

Some sensors needing to be irradiated are simply to big to put in a pneumatic tube, for this and other reasons the Brown Silicon Group also utilizes RINSC's beamport in addition to the rabbit tubes. The beamport is a large cylindrical pipe which goes directly into the reactor (the aluminum vessel which houses the sensors and goes into the pipe can be seen in figure 6.2 (c)). Currently we are using it to irradiate silicon sensors from the HGCAL group along with some test sensors used to monitor the fluence levels across runs. The test structures we are using to monitor the fluence in each run include the HGCAL and DZero cutouts. Additionally iron foils are placed with the sensors. We analyze their activation to further determine what irradiation levels the sensors experienced.

The different sensors are "sandwiched" between layers of kapton film within the

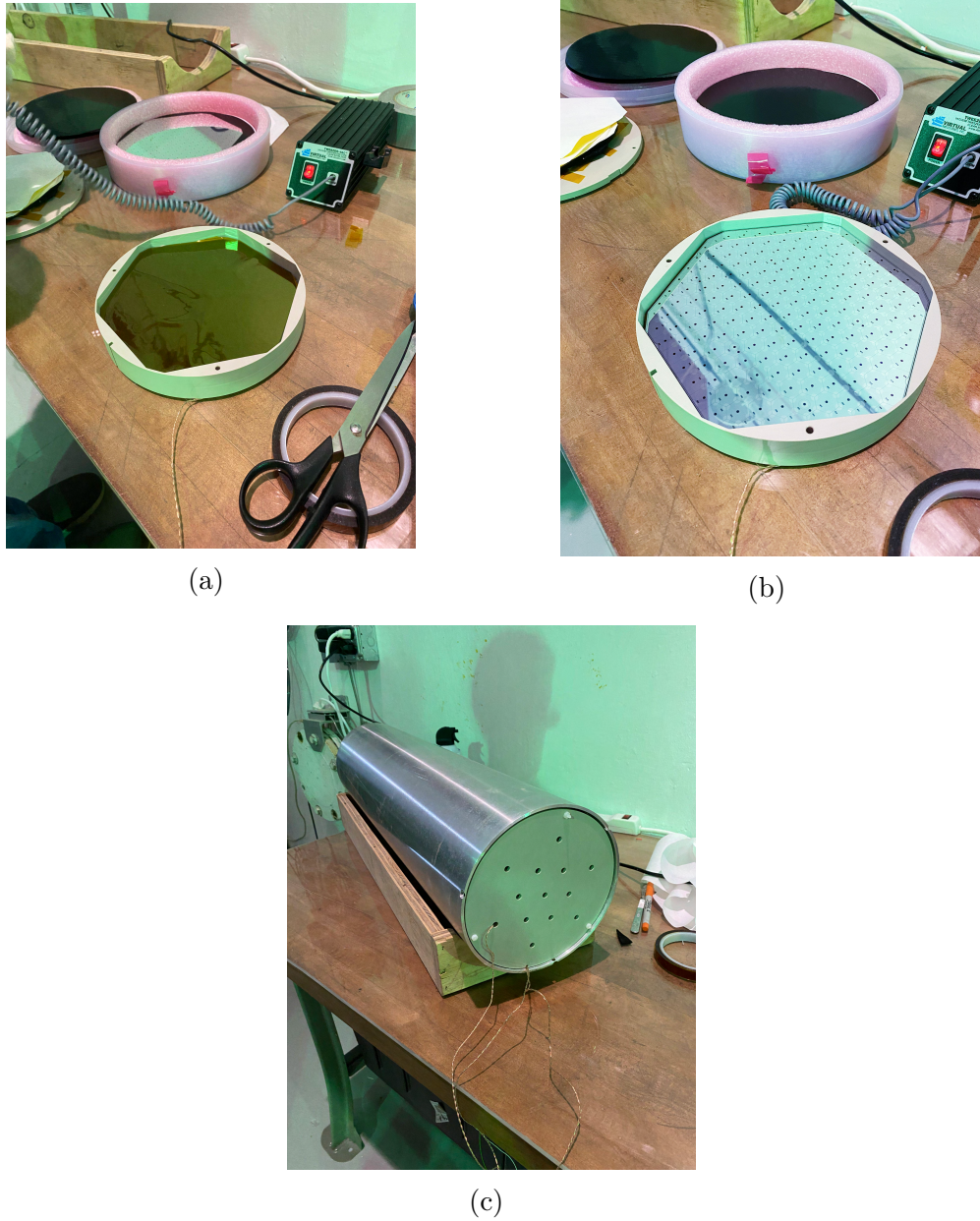


Figure 6.2: (a) Example of a kapton layer separating the different sensors of the beamport tube. (b) Hexagonal HGCAL sensor. (c) Beampore tube fully assembled with temperature sensor wires coming out.

housing container (see figure 6.2 (a) and (b)). There are two primary layers, the front and the back, where naturally the front layer corresponds to the layer which is closest to the reactor core. Also included in each of the layers is a RTD (Resistance Temperature Detector) sensor which is able to record temperatures during irradiation in real time. What we have noticed during different irradiation runs is a discrepancy between anticipated fluence and measured fluence, and also occasionally

a significantly higher measured fluence for the sensors in the back of the beamport tube over the front of the tube. This of course should not be happening, due to the simple fact that the front of the beamport is closer to the neutron flux generated by the reactor core and therefore should register a higher fluence. One of the clues for a possible cause is the temperature the sensors experience during irradiation.

Although the aluminum tube is filled with dry ice (solid CO_2), temperatures during irradiation can sometimes reach $+100^{\circ}C$ for extended periods of time. Of course the reactor core generates Xrays which delivery their energy to nearby objects as heat and so it is the front of the beamport that should experience a higher temperature. our thinking is that there is a concurrent annealing effect occurring during irradiation which is leading to lower measured fluences. Analyzing these two concurrent effects on the HGCAL cutout silicon sensors will be the primary focus of the next chapter.

Chapter 7

Analysis

There are two main sections which comprise this chapter. The first section covers some PIN diode analysis which includes how one may use a PIN diode as a temperature sensor which is then used to inform the method to arrive at a conversion formula between annealing PIN diodes at different temperatures. The second section involves the Hamburg model to infer the accumulated annealing of silicon sensors prior to their arrival at the Brown Silicon Lab. This analysis was used when doing a calibration check between two different CMS irradiation sites; Ljubljana and RINSC (the irradiation site the Brown Silicon group uses). The other part of the Hamburg analysis included in this chapter is the analysis of the concurrent annealing and irradiation effect on the beamport HGCAL cutout silicon sensors.

7.1 PIN Analysis

As mentioned above, this section outlines an analysis of the effect of temperature on unirradiated PIN diodes which was then used to inform us on how best to do an annealing study for PIN diodes. The main question in the temperature study was: "if we place a PIN diode inside of an oven set at a specific temperature, how long does it take for that PIN diode to saturate to that temperature?". We then used the answer from that question to better access how much annealing occurred in one annealing step. We then took that to then find how the effect of annealing on irradiated PIN diodes scale with temperature, and whether that effect scaled exponentially like was found previously for other silicon sensors.

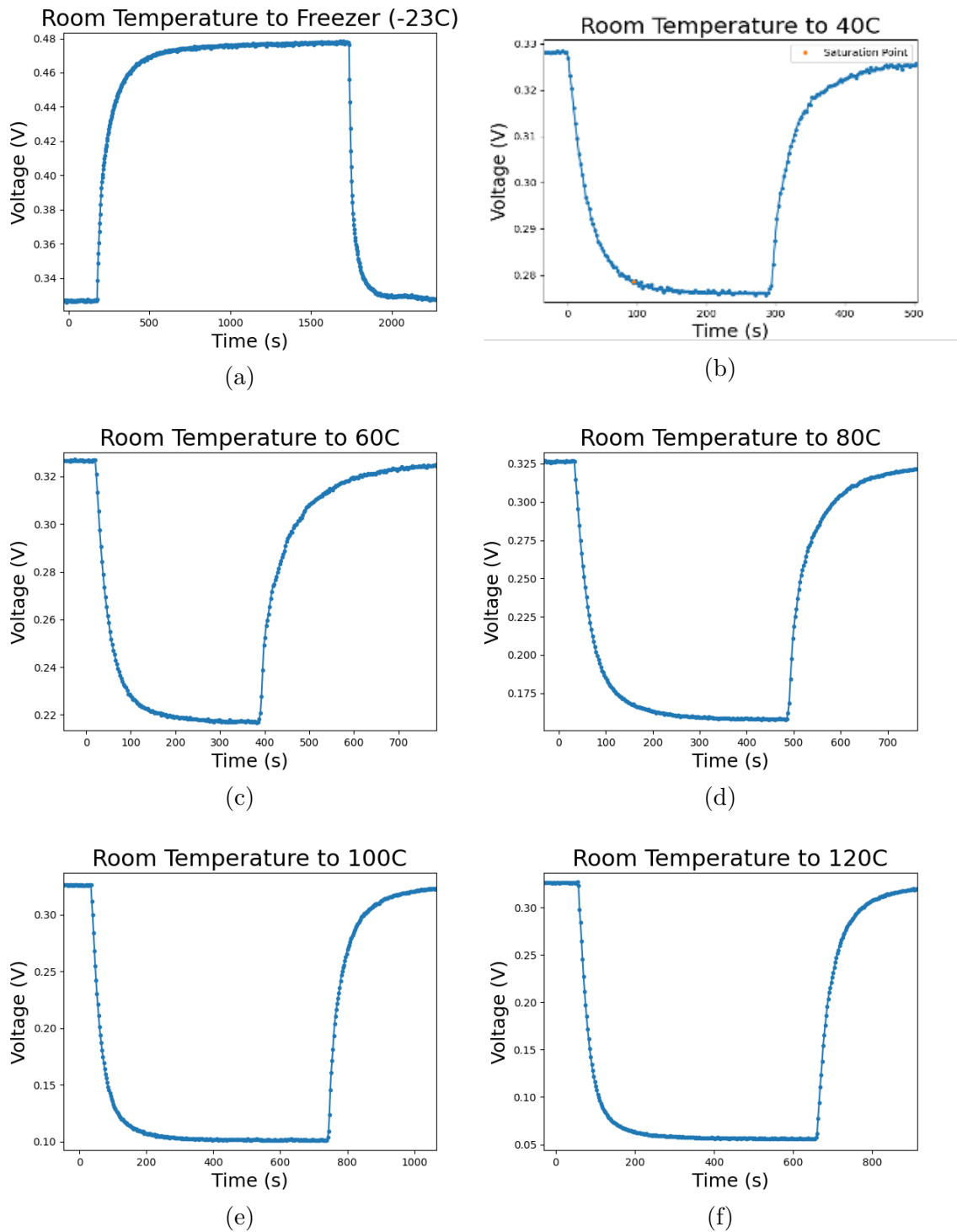


Figure 7.1: Forward voltage (V_f) vs. time for an unirradiated PIN diode

7.1.1 Temperature Study

The method we used for determining the effect of temperature on unirradiated PIN diodes was to measure every second the forward voltage (V_f) response of applying a

$1mA$ pulse for $12ms$. What we found (shown in figure 7.1) was that if we define the saturation forward voltage (V_{sat}) as the value of the forward voltage after prolonged exposure to a specific temperature, then the saturation voltage vs. temperature follows a linear relationship for values of temperature $T \in (-20^{\circ}C, 100^{\circ}C)$.

This result can be seen in figure 7.2, while this was interesting we did not pursue this any further. Instead we changed the method with which we were heating up the PIN diodes within the oven so that the ramp up time plus the ramp down time was less than 1% of the total annealing time. This was important because the value we were interested in, with regard to the PIN diodes, was the effect of cumulative annealing. So ensuring that time quoted at a specific temperature was in fact that time was important. We achieved this by changing annealing from an aluminum tray to a thick aluminum plate which was always within the oven. This ensured that there would be more effective thermal contact which reduced the ramp up time. Once annealed we then placed the PIN diodes onto another aluminum plate at room temperature, we found that by doing this our ramp up and ramp down times would be less than 1% of the annealing time if the annealing steps were greater than 10 minutes.

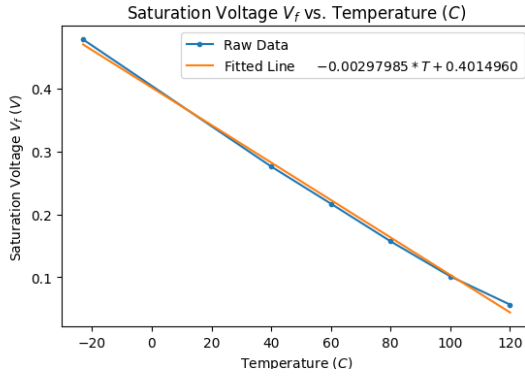


Figure 7.2: Result of unirradiated PIN-thermometer analysis, found that ramp-up-time would significantly affect cumulative annealing time for short-duration annealing if Annealed on surface not already pre-heated to oven temperature.

7.1.2 Annealing Study

The PIN annealing study, as briefly described above, was intended to answer the question of is there a way to convert between different annealing temperatures in a

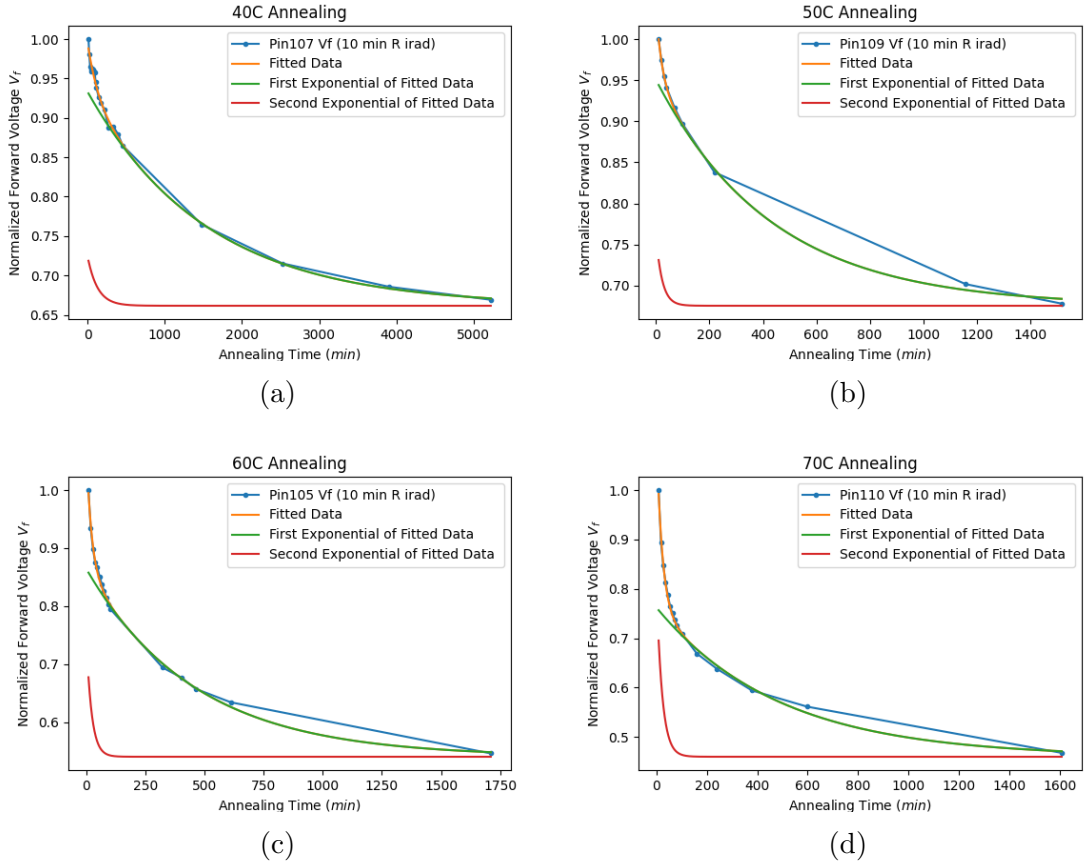


Figure 7.3: Normalized forward voltage (V_f) vs. cumulative annealing time for PIN-diodes for 40°C , 50°C , 60°C and 70°C

simple way. This was relevant to our group because we were curious if there was a way to account for annealing in the way we accounted for annealing for other diodes we worked with. In particular we were interested in being able to integrate over the temperatures experienced by the diode in question in order to come up with a number which we could use to understand the cumulative annealing in a simple way. Getting the data was a simple but time consuming process. The PIN diodes used in this analysis were all from the same rabbit irradiation run. The irradiation run was also very short at 10 minutes with an approximate fluence reading of $1.5e15 \text{ n/cm}^{-2}$, we decided to use PIN diodes from such a run because we found that concurrent annealing and irradiation effects were minimized for low fluences. Annealing temperatures were chosen based on the temperatures sensors experienced in the rabbit (since we only use the PIN diodes in the rabbit) and at the time our temperature stickers were indicating that the maximum temperature experienced

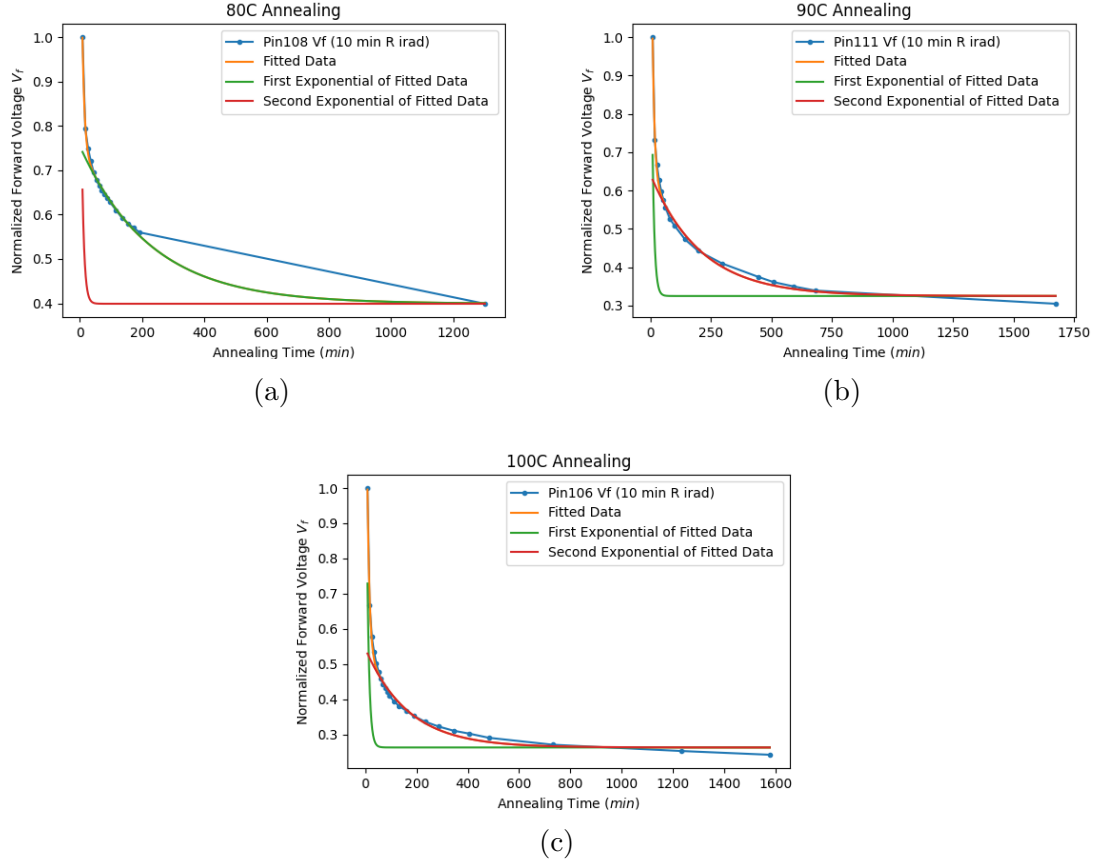


Figure 7.4: Normalized forward voltage (V_f) vs. cumulative annealing time for PIN-diodes for $80^{\circ}C$, $90^{\circ}C$ and $100^{\circ}C$

was $70^{\circ}C$. The results of the analysis and can be seen in figure 7.3 and 7.4, in these graphs we normalized to the initial forward voltage of the PIN diode without any annealing. We decided to fit the data to a sum of two exponential of the form:

$$f(x) = a \cdot e^{b \cdot t} + c \cdot e^{d \cdot t} \quad (7.1)$$

where a, b, c and d are all free parameters, we did this for each of the annealing temperatures. Then, to be able to compare the temperatures to one another, we decided to compare the annealing temperature which had the most robust data to the others. This turned out to be the $100^{\circ}C$ data, and the form of the function we used to match the others was the following.

$$f_{100^{\circ}C}(x) \rightarrow f(a(t - b)) \quad (7.2)$$

the intuition behind the two parameters is that “a” accounts for the strength of the annealing (assuming an exponential response in temperature) while “b” accounts for

any pre-annealing that occurred in the reactor. The results of the parameter fitting is summarized in the table 7.1

Annealing Temperature	a [$\frac{1}{t}$]	b [t]
40°C	1.88e-03	-2.018e+03
50°C	7.19e-03	-4.58e+02
60°C	1.40e-02	-3.37e+02
70°C	3.08e-02	-1.68e+02
80°C	0.11	-32.50
90°C	0.28	-10.44
100°C	1.06	7.14

Table 7.1: Annealing Fitting Parameters

The result of plotting the exponential scale factor (a) to annealing temperature can be seen in figure 7.5, where indeed we see an exponential relationship between that scale factor and the different annealing temperatures. The function which was fitted to the data was the same as that which we used for D0 diodes, with this function we can now (listed in the legend of 7.5) compare annealing temperatures to themselves and then use that information to estimate the fluence when the diode came first out of the reactor.

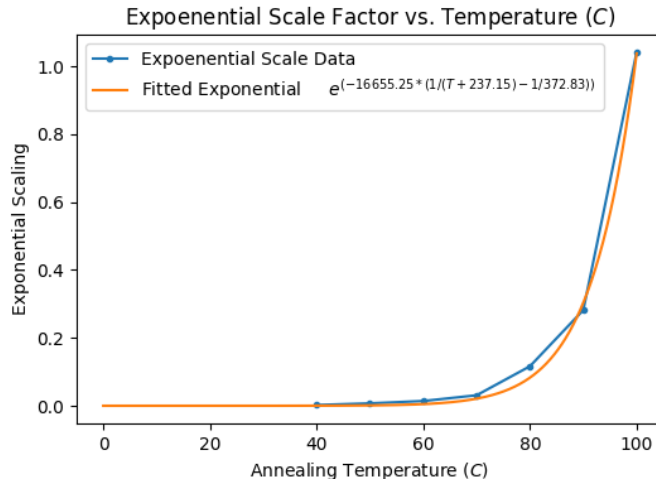


Figure 7.5: Exponential scale factor vs. temperature for PIN diodes

7.2 Hamburg Model Analysis

This section deals with two instances where we annealed irradiated diodes and then used the Hamburg Model on that data to infer information about the annealing which either occurred during transportation to the Brown Silicon Lab or annealing which occurred during the irradiation process. The first part of this analysis will speak about the use of the Hamburg Model on diodes which we suspected were annealed on transit to our lab. The second part will consider the effects of concurrent annealing and irradiation effects, this is of concern for the Brown Silicon Group and the HGCAL group because we both analyze properties of silicon sensors irradiated in the beamport at RINSC. This particular irradiation location experiences high temperatures throughout irradiation even when precautions are made (like filling the tube with dry ice), so better understanding how these effects are combined is critical to continued use of the beamport at RINSC and which may further lead to improvements on how those sensors are irradiated or greater understanding on the play between concurrent irradiation and annealing.

7.2.1 Ljubljana Diodes

Two of the main irradiation locations for the CMS group are RINSC and Ljubljana, for that reason there was an effort made to cross calibrate these two locations quoted fluences in order to have greater consistency within the collaboration. During this cross calibration check there were PIN and DZero diodes sent to Ljubljana irradiated at four separate fluences ($6.5e14$, $1.5e15$, $2.5e15$ and $5e15\text{ }n/cm^{-2}$) and we were to measure those diodes using our lab equipment to see how well our values lined up with what Ljubljana quoted they should be. Initially there was discrepancy between the two values, and so the Brown Silicon group looked to see what might be the cause. There were a few candidates for what might be reason for this discrepancy, those ideas were:

1. Our volume measurement for D0 diode are not accurate
2. Diodes over irradiated, therefore results not accurate

- Annealing occurred during transportation to Brown, which caused lower fluence measurements

The first point was looked into, and we then found that the depth value we were using for the diode was off, which did lead to an improvement (to be discussed in section 8.1). The second point was immediately apparent, for only the $6.5e14 \text{ MeVn/cm}^{-2}$ diodes were depleting below our maximum voltage of 1100V's. Therefore, our estimates for those higher fluence values could only be interpreted as lower bounds. Then, given that the transportation box (which originally had dry ice inside) did not contain dry ice, we decided to pursue the third point.

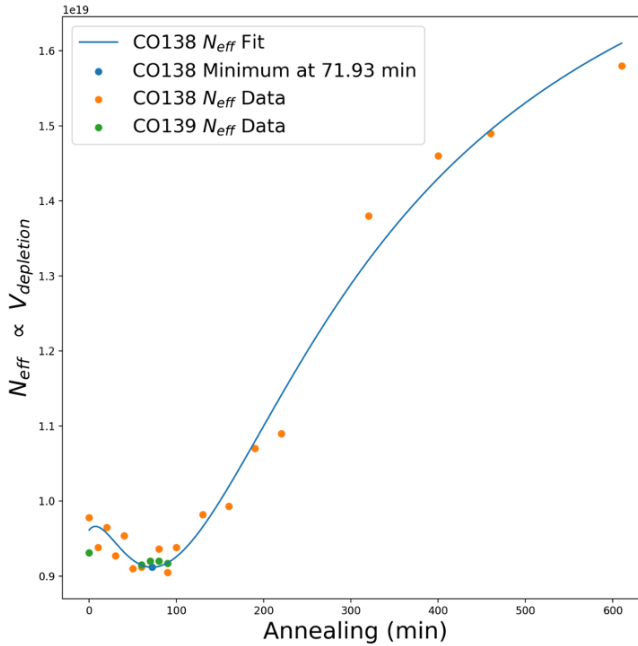


Figure 7.6: Ljubljana Hamburg analysis of DZero diodes to determine possible transportation annealing en route to Brown University from Slovenia

Unfortunately there was no remote temperature sensor within the transportation box so we only had rough estimates of what the temperature likely was. For this reason we resorted to the Hamburg model to see if we could estimate what annealing occurred based on the minimum of the N_{eff} vs. Annealing Time graph. For D0's we have measured in the past in our own lab, and D0's similarly measured and analyzed at Fermilab, we expect a minimum in that data to occur at 80 minutes of annealing

at $60^{\circ}C$ - any deviation from that would indicate annealing during transportation to Brown.

We decided to anneal a D0 diodes from the $6.5e14 \text{ MeVn/cm}^{-2}$ batch at 10 minute increments up to 100 minutes, and then open up the step sizes once a lot of the subtle changes in N_{eff} subsided. The depletion voltage was measured for each of these annealing steps, and the results were fed into equation 3.5 to arrive at figure 7.6. Based on the minimum of the Hamburg fit occurring at 71.93 minutes, we can be reasonable sure that approximately 8 minutes of annealing occurred on the trip from Slovenia to Providence, Rhode Island. When converting between annealing temperatures, we find that 8 minutes of annealing at $60^{\circ}C$ is equivalent to 33 hours at $20^{\circ}C$ - a reasonable estimate for the length of travel time without dry ice. These results are interpreted into the general results of the RINSC-Ljubljana/JSI cross calibration in section 8.1.

7.2.2 HGCAL Diodes

This section, as mentioned earlier, will cover the Hamburg Model analysis results on the HGCAL cutout diodes which were irradiated in the beampipe at the RINSC irradiation facility. Within the different irradiation runs were also some D0 diodes (largely ineffective at giving reliable fluence estimates for irradiation times greater than 25 minutes due to the depletion voltage being greater than the 1100V limit), iron foils and full scale HGCAL hexagonal silicon diodes. Photos of this arrangement can be found in section 6.2. The objective of this analysis was to try and shine a light on the interplay between annealing and irradiation during irradiation. Some of the HGCAL rounds experienced as much as 10,000 minutes of equivalent annealing at $60^{\circ}C$ which would of course affect the resulting measured fluence. The following grouping of plots constitute seven different irradiation runs, each of the runs will be briefly described before a full analysis of the results is discussed in section 8.2.

For the following analysis I will think of N_{eff} as a function of annealing time $N_{eff}(t)$, where $t_{min}^{60^{\circ}C}$ is the cumulative annealing at $60^{\circ}C$ which resulted in a minimum in $N_{eff}(t)$. Also, $\Phi_{eq}(t_{min}^{60^{\circ}C})$ is the fluence value which is extracted when using the

data from the minimum of the $N_{eff}(t)$ curve. Finally, I will define A_{60^oC} as the cumulative equivalent annealing at 60^oC .

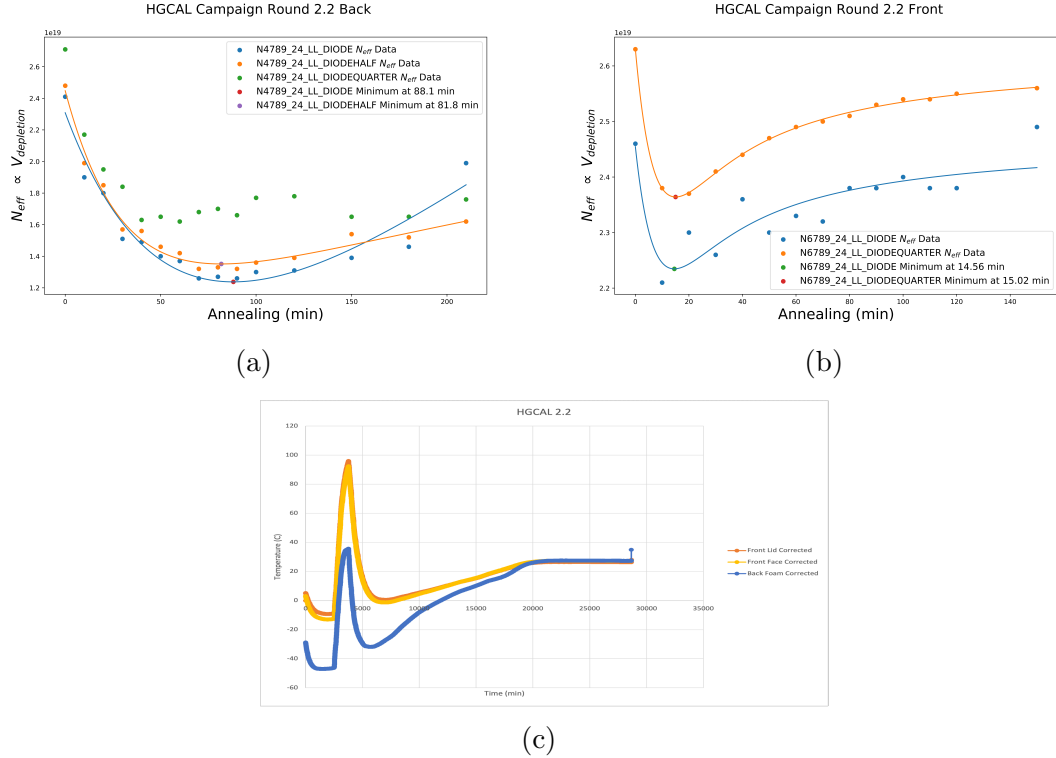


Figure 7.7: Hamburg analysis of HGCAL diodes irradiated at RINSC for 43 minutes. (a) HGCAL diode at back of beamport, (b) HGCAL diode at front of beamport, (c) temperature profile from start of irradiation to them being pulled out.

In HGCAL round 2.2 (figure 7.7) we can notice that the front diode experienced a higher temperature with a cumulative equivalent annealing at 60^oC of 504 minutes whereas the back diode experienced approximately 6.01 minutes of cumulative equivalent annealing at 60^oC .

Diode	Location	$t_{min}^{60^oC}$	$\Phi_{eq}(t_{min}^{60^oC})$	A_{60^oC}
DIODE	BP Front	14.56	9.54E+14	504
DIODEQUARTER	BP Front	15.02	1.08E+15	504
DIODE	BP Back	88.1	1.35E+15	6.01
DIODEHALF	BP Back	81.8	1.28E+15	6.01
DIODEQUARTER	BP Back	NA	(taken at 60^oC) 1.61E + 15	6.01

Table 7.2: HGCAL Round 2.2 Extracted Hamburg Values

Therefore we expect the minimum of N_{eff} to occur at a lower cumulative annealing for the front diodes, this is in-fact the case and we can see that the DIODE

for the front HGCAL cutout saw a minimum occur at 15.02 minutes where DIODE on the back HGCAL cutout had a minimum at 88.1. Although we expect a higher measured fluence for the cutout on the front of the beamport, the opposite is the case. From table 7.2 we can see that the fluence estimate is nearly 30% higher for the back DIODE than for the front.

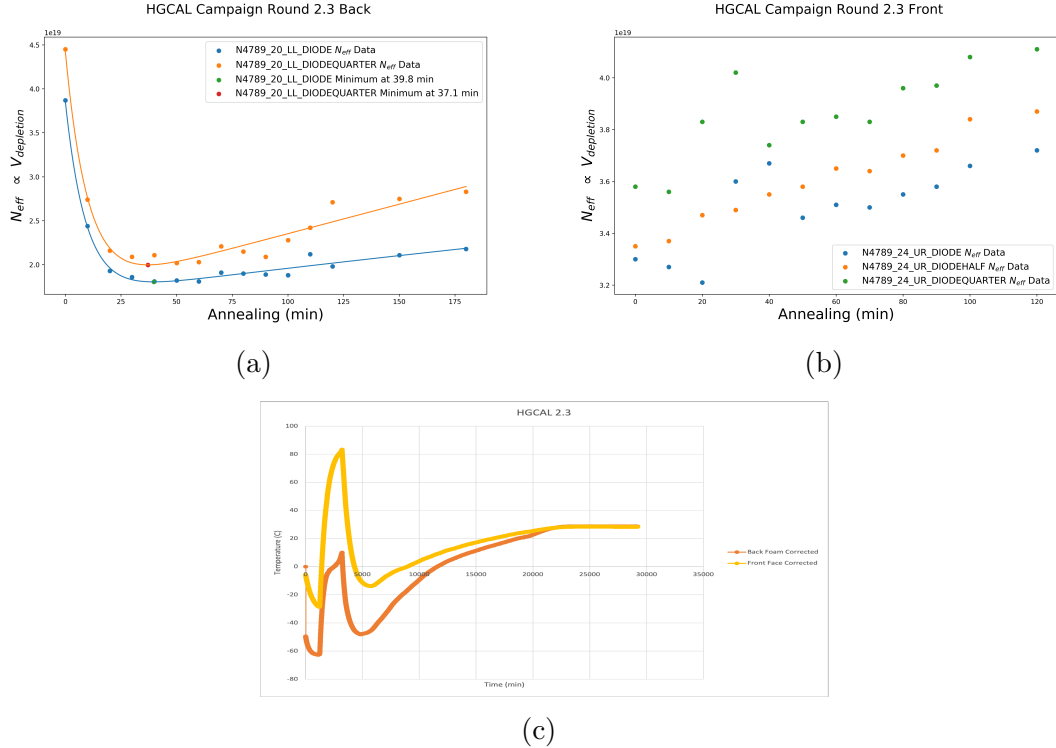


Figure 7.8: Hamburg analysis of HGCAL diodes irradiated at RINSC for 86 minutes

In HGCAL round 2.3 (seen in figure 7.8) we can see a very close agreement between the two diodes on the BP_Back HGCAL cutout while the BP_Front diodes seem to have experienced so much annealing during irradiation that they past the minimum ($N_{eff}(t_{min}^{60^{\circ}C})$) prior to being brought back from RINSC.

Diode	Location	$t_{min}^{60^{\circ}C}$	$\Phi_{eq}(t_{min}^{60^{\circ}C})$	$A_{60^{\circ}C}$
DIODE	BP Front	0	2.08E+15	374
DIODEHALF	BP Front	0	2.15E+15	374
DIODEQUARTER	BP Front	0	2.35E+15	374
DIODE	BP Back	39.8	2.78E+15	5.62
DIODEQUARTER	BP Back	37.1	3.09E+15	5.62

Table 7.3: HGCAL Round 2.3 Extracted Hamburg Values

This is confirmed by the data in table 7.3 which indicates the front diodes

experienced 374 minutes of cumulative annealing at $60^{\circ}C$ to the back diodes 5.62 minutes. Although the cumulative annealing analysis would seem to indicate that $N_{eff}(t_{min}^{60^{\circ}C})$ should occur at ~ 70 minutes, we instead find that it occurs at ~ 40 minutes. The fluence estimates for this round were again flipped from what we would have expected them to be, with the front DIODE measuring $2.08 \cdot 10^{15} n/cm^{-2}$ to the back DIODE's $2.78 \cdot 10^{15} n/cm^{-2}$, a 33% difference between the two.

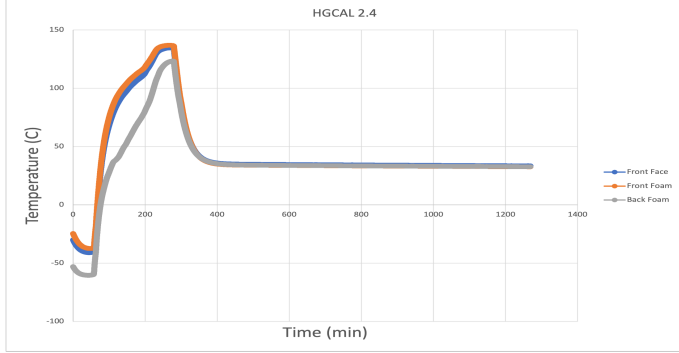


Figure 7.9: Hamburg analysis of HGCAL diodes irradiated at RINSC for 216 minutes

HGCAL round 2.4 was irradiated for significantly longer than any of the other rounds, and due to the prolonged exposure to the reactor core (216 minutes) there was a few unintended consequences. The plastic bags that we put the diodes into shrunk in the heat, and the bag for the front diode snapped in half as a result of that shrinking. When integrating the temperature profile, we found that the back of the beamport received a cumulative equivalent annealing of 27,252 minutes while the front received 106,709 minutes.

Although the temperature sensors and the HGCAL cutout from the back of the beamport did survive the extended exposure, we were not able to identify a depletion voltage on the probe station and so the results from this annealing analysis were not included in the overall results. The reason for doing so is that the depletion voltage is proportional to N_{eff} , and so if the depletion voltage is registering well above 1100V's (how far we can bias the diode) then we cannot determine the true value of N_{eff} . Additionally not much can be said about the measured fluence values, we would be under estimating from our lack of knowledge in the depletion voltage but also over estimating from because of how much annealing the sensors experienced in the reactor.

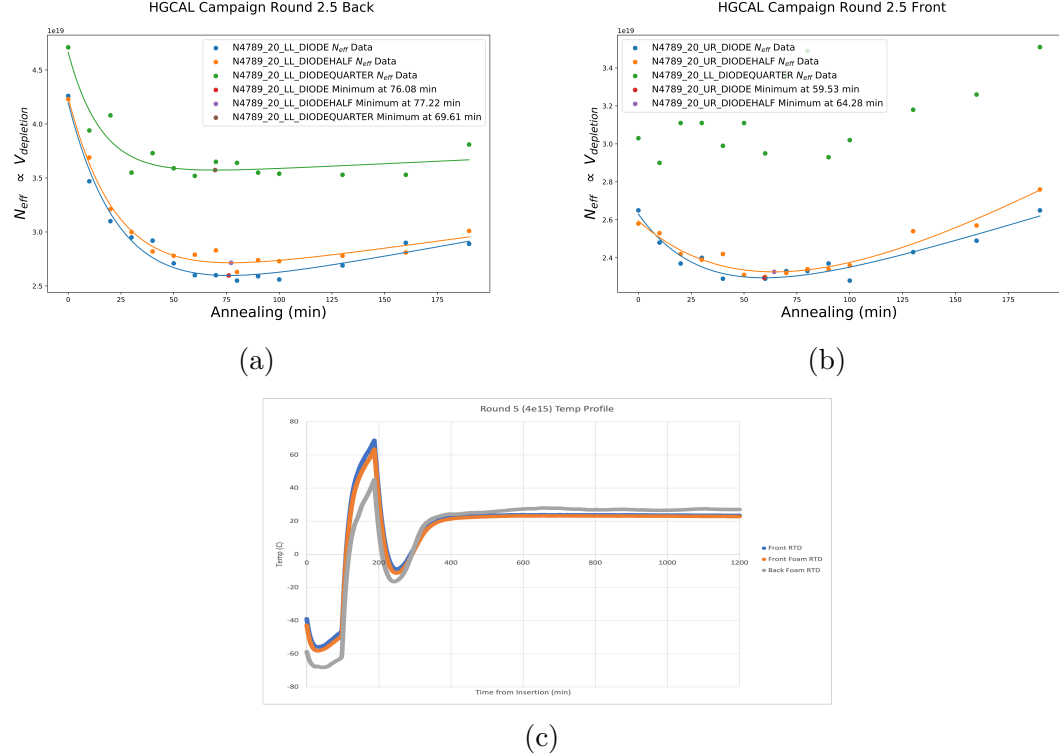


Figure 7.10: Hamburg analysis of HGCAL diodes irradiated at RINSC for 86 minutes

HGCAL round 2.5 was irradiated for 86 minutes, and although the diodes on the front and back experienced very different cumulative equivalent annealing (69.17 minutes for the front and 11 minutes for the back) their N_{eff} vs. Annealing graphs showed very similar results.

Diode	Location	$t_{min}^{60^{\circ}C}$	$\Phi_{eq}(t_{min}^{60^{\circ}C})$	$A_{60^{\circ}C}$
DIODE	BP Front	59.53	2.81E+15	69.17
DIODEHALF	BP Front	64.28	2.90E+15	69.17
DIODEQUARTER	BP Front	NA	3.31E+15	69.17
DIODE	BP Back	79.08	3.09E+15	11
DIODEHALF	BP Back	77.22	3.07E+15	11
DIODEQUARTER	BP Back	69.61	3.52E+15	11

Table 7.4: HGCAL Round 2.5 Extracted Hamburg Values

In table 7.4 we can see that the fluence value for the front DIODE was in fact higher than the back, which is what we expect should happen. Its not quite clear what happened in BP_Front DIODEQUARTER, though since this is the smallest diode it is not cause for concern and should be dismissed.

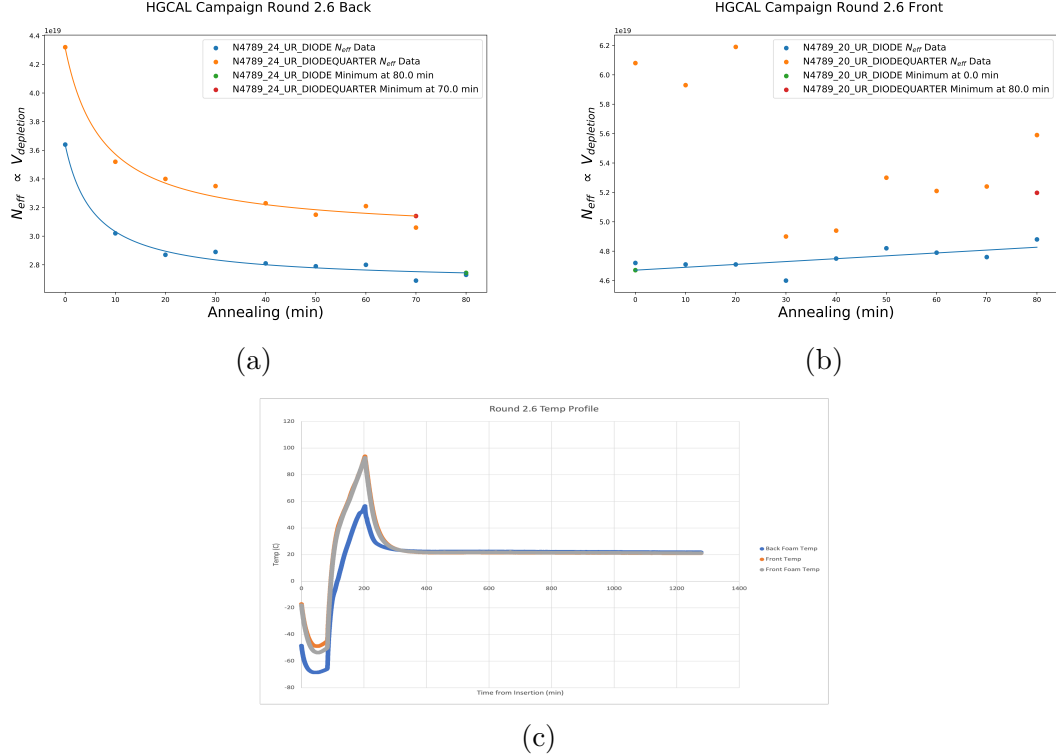


Figure 7.11: Hamburg analysis of HGCAL diodes irradiated at RINSC for 118 minutes

HGCAL round 2.6 was another one of the longer irradiation runs at 118 minutes, and we can see the effects of the longer irradiation in the front HGCAL cutout.

Diode	Location	$t_{min}^{60^{\circ}C}$	$\Phi_{eq}(t_{min}^{60^{\circ}C})$	$A_{60^{\circ}C}$
DIODE	BP Front	0	2.86E+15	739.3
DIODEQUARTER	BP Front	0	3.35E+15	739.3
DIODE	BP Back	80.0	3.68E+15	20.6
DIODEQUARTER	BP Back	70.0	4.16E+15	20.6

Table 7.5: HGCAL Round 2.6 Extracted Hamburg Values

In table 7.5 we can see what is partially reflected in figure 7.11, that a cumulative equivalent annealing of 739.3 minutes was more than significant enough to push N_{eff} into the region where each successive annealing step resulted in a higher N_{eff} . Looking at the diodes in the back of the beamport we register a cumulative equivalent annealing of 20.6 minutes and so suspect a minimum to occur at around 60 minutes. Further measurements would be needed for the back diode to fully characterize the minimum, but during the measurement of the DIODE 80 minute annealing the chip experienced a failure and no longer was able to be measured.

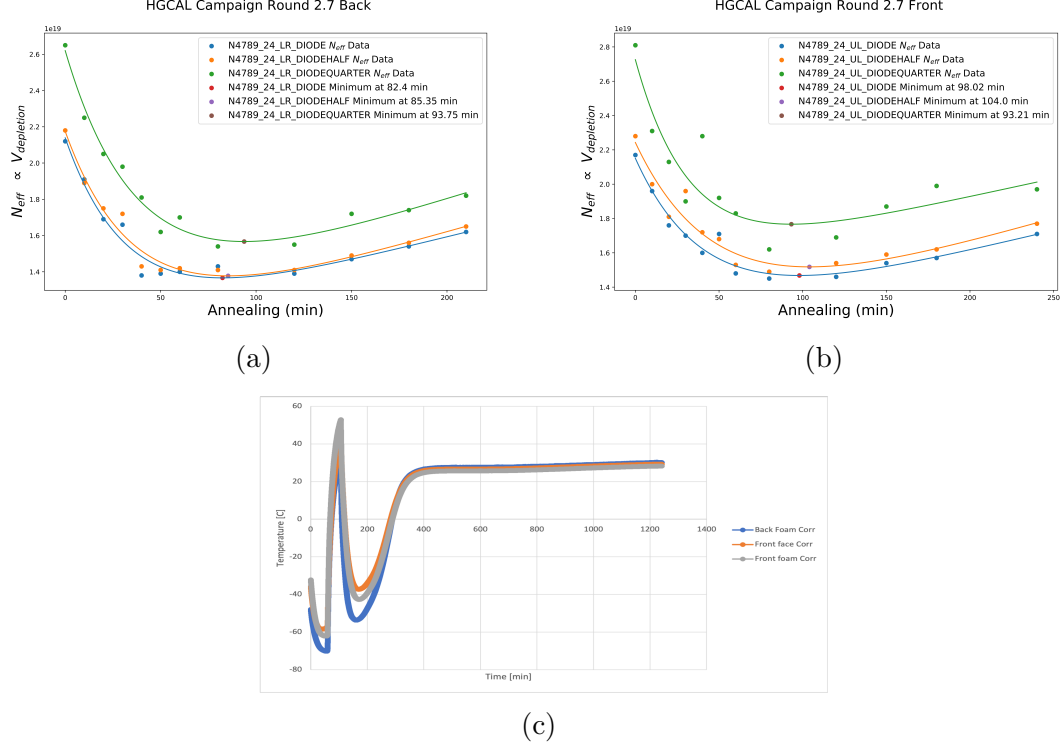


Figure 7.12: Hamburg analysis of HGCAL diodes irradiated at RINSC for 43 minutes

In the above figures 7.12 we can see the results of the Hamburg analysis for HCGAL 2.7, a shorter irradiation run at 43 minutes. The Hamburg fit for both of the data have excellent indication for a minimum and those values are reflected in the table below. Again we notice that the minimum has shifted further back for the diodes which experienced more annealing and in this case it was the front diodes which were annealed more. Additionally the fluence estimates are also likewise what we expect with the front measuring a higher fluence.

Diode	Location	$t^{60^\circ C}_{min}$	$\Phi_{eq}(t^{60^\circ C}_{min})$	$A_{60^\circ C}$
DIODE	BP Front	98.02	1.51E+15	12.6
DIODEHALF	BP Front	104.0	1.57E+15	12.6
DIODEQUARTER	BP Front	93.21	1.70E+15	12.6
DIODE	BP Back	82.4	1.27E+15	13.09
DIODEHALF	BP Back	85.35	1.40E+15	13.09
DIODEQUARTER	BP Back	93.75	1.53E+15	13.09

Table 7.6: HGCAL Round 2.7 Extracted Hamburg Values

In table 7.6 we can see that once again the front diode measured a higher fluence than the back diodes, and they both experienced very similar cumulative equivalent

annealing at 12.6 minutes for the front cutout and 13.09 for the back. It does look like with further measurements more could be said, if I had more time to measure this in my mind would be the run to do.

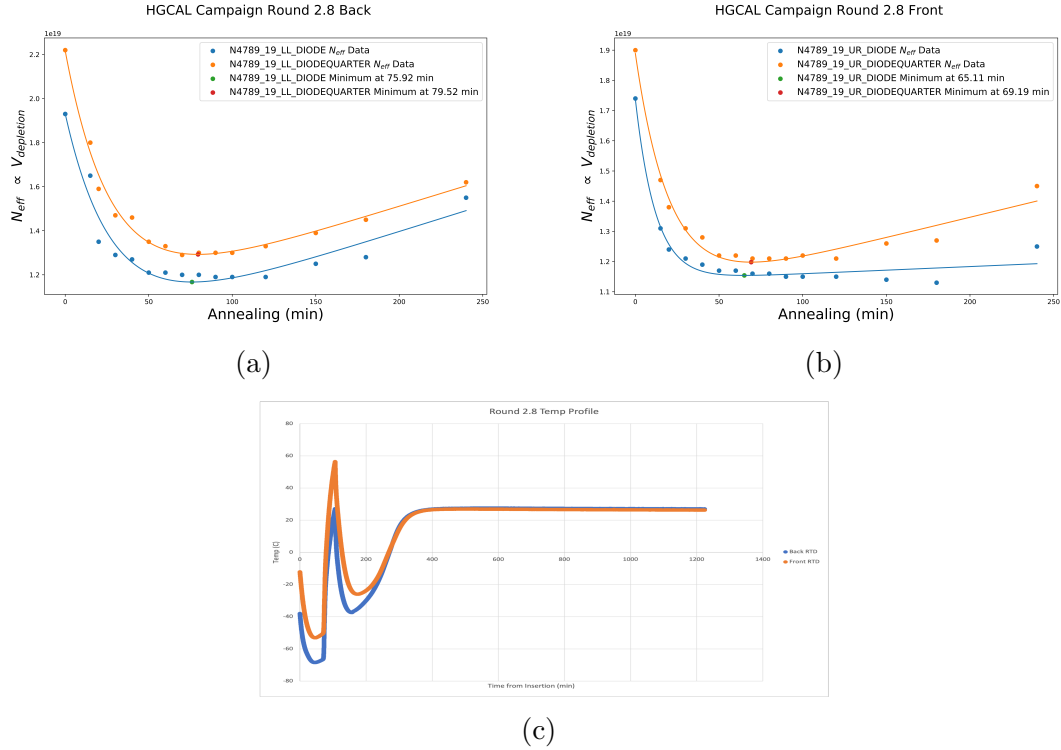


Figure 7.13: Hamburg analysis of HGCAL diodes irradiated at RINSC for 32 minutes

The final HGCAL round I will be discussing in 2.8, this round was irradiated for 43 minutes and the Hamburg for these diodes were especially well behaved. In this round we saw that the front experienced greater equivalent cumulative annealing and this is reflected in the minimum for $N_{eff}(t)$ being lower than for the diodes in the back of the beamport.

Diode	Location	$t_{min}^{60^{\circ}C}$	$\Phi_{eq}(t_{min}^{60^{\circ}C})$	$A_{60^{\circ}C}$
DIODE	BP Front	65.11	1.08E+15	14.4
DIODEQUARTER	BP Front	69.19	1.22E+15	14.4
DIODE	BP Back	75.92	1.05E+15	10.9
DIODEQUARTER	BP Back	79.52	1.11E+15	10.9

Table 7.7: HGCAL Round 2.8 Extracted Hamburg Values

In table 7.7 we can see again that the equivalent cumulative annealing were very similar for both the front and back diodes, at 14.4 minutes for the front and 10.9

minutes for the back. Additionally the fluence measurements were very closer for both of the larger diodes with the front DIODE measuring $1.08 \cdot 10^{15} \text{ } n/cm^{-2}$ to the back DIODE's $1.05 \cdot 10^{15} \text{ } n/cm^{-2}$.

Chapter 8

Conclusions

The following two sections conclude this thesis, the first section will serve to finalize the JSI/Ljubljana-RINSC cross calibration analysis. The second section will summarize the data gathered on the Hamburg analysis of seven irradiation runs. Finally a discussion on possible future directions, primarily with respect to the question of the effect of concurrent annealing and irradiation on silicon sensors, will close this paper.

8.1 RINSC-Ljubljana Cross Calibration

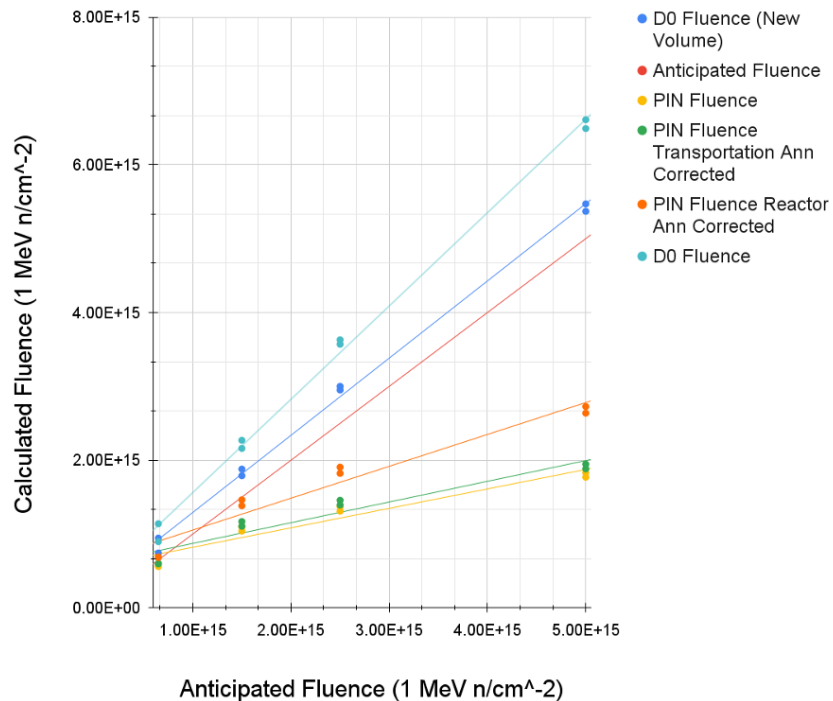


Figure 8.1: Calculated fluence of PIN and D0 diodes vs. Ljubljana anticipated values

The above plot (figure 8.1) shows both the PIN and D0 diodes from the RINSC-

Ljubjana Cross Calibration runs with their respective fluence values. On the vertical axis we see the measured fluence values while on the horizontal axis we can see the fluence values that Ljubjana irradiated them to in their facility. The red line in the center of the graph is the line that corresponds with our measurements identically equaling those values given to us by Ljubjana.

In the figure we can see the initial D0 fluence estimate in light blue, which is far above the estimate given to us by Ljubjana, though linear in the response. From here we investigated further and found that our value for the volume of the diode was off which lead to our fluence estimate for the D0 diodes indicated by the blue line. This we found to be within the error and so felt we had achieved agreement with the fluence results of Ljubjana. Correcting for the annealing experienced during travel from Slovenia to Rhode Island resulted in less than a 1% change, so this was not included in the final values.

For the PIN diodes, we confirmed a fact that we noticed within our own measurements at RINSC, that the fluence results for PIN diodes irradiated to values over $\sim 1.0 \cdot 10^{15} n/cm^{-2}$ simply do not scale linearly. Therefore for irradiation runs which require precise measurements of fluence above that range, we simply choose not to rely on PIN diodes and instead utilize iron foils and D0 diodes. Although, we do use PIN diodes for rough approximations of relative fluence between adjacent diodes like when assessing the relative fluence levels across and along rabbit faces.

8.2 Effects of Concurrent Annealing and Irradiation

In figure 8.2 we can see a log-linear graph which shows equivalent cumulative annealing vs. $N_{eff}(t_{min}^{60^{\circ}C})$ for the HGCAL diodes from the analysis portion of this thesis. There are two major outliers from HGCAL Round 2.3 BP_Back which experienced 5.62 minutes of cumulative annealing, though whose minimum were very close to 40 minutes. Other than those two points it does look like there is an exponential relation between a higher equivalent cumulative annealing and a lower $N_{eff}(t_{min}^{60^{\circ}C})$,

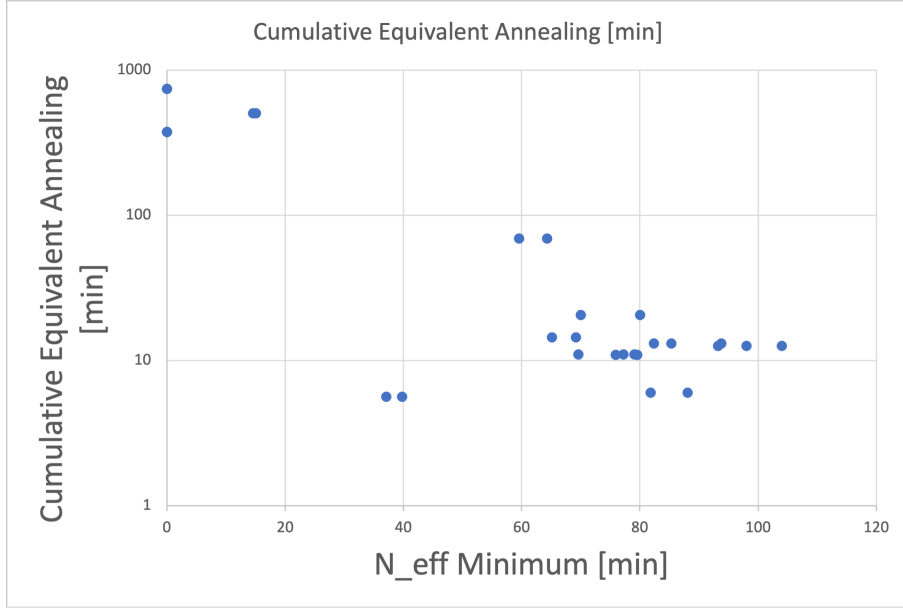


Figure 8.2: Equivalent cumulative annealing vs. $N_{eff}(t_{min}^{60^{\circ}C})$ for HCGAL diodes irradiated at RINSC

though more data would be needed to better characterize that relation and also rule out why there was an issue with 2.3 back.

8.3 Future Work

Further investigation into the effects of concurrent annealing and irradiation is absolutely necessary for better understanding the state of the silicon sensors we are receiving from RINSC. I think that more data should be taken for a variety of fluences and if possible different heating regimes as well. It is very reasonable to imagine that the effect of annealing early in the irradiation process is less important to the joint effect than annealing which occurs later, so possibly weighing the different regimes could be one angle of attacking the problem.

Bibliography

- [1] W. Adam et al. ‘P-Type Silicon Strip Sensors for the new CMS Tracker at HL-LHC’. In: *Journal of Instrumentation* 12.06 (June 2017), P06018–P06018. doi: [10.1088/1748-0221/12/06/p06018](https://doi.org/10.1088/1748-0221/12/06/p06018). URL: <https://doi.org/10.1088/1748-0221/12/06/p06018>.
- [2] Adundovi. *A P-N Junction in Thermal Equilibrium*. URL: https://en.wikipedia.org/wiki/P%28E2%80%93n_junction.
- [3] Alexander Furgeri. ‘Quality assurance and irradiation studies on CMS silicon strip sensors’. PhD thesis. Karlsruhe U., 2006.
- [4] Julie Haffner. ‘The CERN accelerator complex. Complexe des accélérateurs du CERN’. In: (Oct. 2013). General Photo. URL: <https://cds.cern.ch/record/1621894>.
- [5] M.R. Hoeferkamp et al. ‘Application of p-i-n photodiodes to charged particle fluence measurements beyond 10^{15} 1-MeV-neutron-equivalent/cm²’. In: *Nuclear Instruments and Methods in Physics Research Section A: Accelerators, Spectrometers, Detectors and Associated Equipment* 890 (2018), pp. 108–111. ISSN: 0168-9002. doi: <https://doi.org/10.1016/j.nima.2018.02.070>. URL: <https://www.sciencedirect.com/science/article/pii/S0168900218302249>.
- [6] Gerhard Lutz. *Semiconductor Radiation Detectors*. Berlin: Springer, 1999. URL: <https://cds.cern.ch/record/887388>.
- [7] Ricardo Marco-Hernandez. ‘A Portable Readout System for Microstrip Silicon Sensors (ALIBAVA)’. In: *IEEE Transactions on Nuclear Science* 56.3 (2009), pp. 1642–1649. doi: [10.1109/TNS.2009.2017261](https://doi.org/10.1109/TNS.2009.2017261).
- [8] Marius Metzler. ‘Irradiation studies on n-in-p silicon strip sensors in the course of the CMS Phase-2 Outer Tracker Upgrade’. PhD thesis. Karlsruhe Institute of Technology (KIT), 2020.

- [9] Michael Moll. ‘Displacement Damage in Silicon Detectors for High Energy Physics’. In: *IEEE Transactions on Nuclear Science* 65.8 (2018), pp. 1561–1582. DOI: [10.1109/TNS.2018.2819506](https://doi.org/10.1109/TNS.2018.2819506).
- [10] Michael Moll. ‘Radiation damage in silicon particle detectors: Microscopic defects and macroscopic properties’. PhD thesis. Hamburg U., 1999.
- [11] Jason Röhr. ‘Electron Transport in Solution Processed Antimony Sulphide Thin Films made from a Xanthate Precursor’. PhD thesis. Sept. 2014. DOI: [10.13140/RG.2.2.29530.39366](https://doi.org/10.13140/RG.2.2.29530.39366).
- [12] Leonardo Rossi et al. *Pixel detectors: from fundamentals to applications*. Particle acceleration and detection. Berlin: Springer, 2006. DOI: [10.1007/3-540-28333-1](https://doi.org/10.1007/3-540-28333-1). URL: <https://cds.cern.ch/record/976471>.
- [13] Tai Sakuma. ‘Cutaway diagrams of CMS detector’. In: (May 2019). URL: <https://cds.cern.ch/record/2665537>.
- [14] *Silicon Pixels Sensors at CMS*. URL: <https://home.cern/science/accelerators/large-hadron-collider>.
- [15] *The High-Luminosity large Hadron Collider*. URL: <https://home.cern/resources/faqs/high-luminosity-lhc>.
- [16] *The Large Hadron Collider*. URL: <https://home.cern/science/accelerators/large-hadron-collider>.
- [17] V A.J Van Lint et al. ‘Mechanisms of radiation effects in electronic materials. Vol. 1’. In: (Jan. 1980). URL: <https://www.osti.gov/biblio/6854931>.
- [18] Pascal Vanlaer et al. ‘The Phase-2 Upgrade of the CMS Tracker’. In: 2017.
- [19] L. Wiik-Fuchs et al. ‘Annealing studies of irradiated p-type sensors designed for the upgrade of ATLAS phase-II strip tracker’. In: *Nuclear Instruments and Methods in Physics Research Section A: Accelerators, Spectrometers, Detectors and Associated Equipment* 924 (2019). 11th International Hiroshima Symposium on Development and Application of Semiconductor Tracking Detectors, pp. 128–132. ISSN: 0168-9002. DOI: <https://doi.org/10.1016/j.nima.2018.10.014>. URL: <https://www.sciencedirect.com/science/article/pii/S0168900218313299>.

- [20] Renate Wunstorf. ‘Systematische Untersuchungen zur Strahlenresistenz von Silizium-Detektoren für die Verwendung in Hochenergiephysik-Experimenten’. University of Hamburg, Diss., 1992. Dr. Hamburg: University of Hamburg, 1992. URL: <https://bib-pubdb1.desy.de/record/153817>.

Appendix A

Code and Data Location

1. GitHub CMS Folder:

https://github.com/AndrewTKent/CERN_CMS_Silicon_Sensor

2. Annealing Temperature Conversion:

https://github.com/AndrewTKent/CERN_CMS_Silicon_Sensor/tree/main/Diodes/DZero/Annealing_Conversion

3. HGCAL Hamburg Analysis:

https://github.com/AndrewTKent/CERN_CMS_Silicon_Sensor/tree/main/Diodes/HGCAL/Hamburg_Analysis

4. Alibava Annealing Studies:

https://github.com/AndrewTKent/CERN_CMS_Silicon_Sensor/tree/main/Diodes/Halfmoon/Annealing

5. Ljubljana vs. Rinsc Analysis:

https://github.com/AndrewTKent/CERN_CMS_Silicon_Sensor/tree/main/Diodes/Ljubljana_Diodes

6. Pin Diodes:

https://github.com/AndrewTKent/CERN_CMS_Silicon_Sensor/tree/main/Diodes/Pins